Contents lists available at ScienceDirect

Remote Sensing of Environment

journal homepage: www.elsevier.com/locate/rse

Analysis of SAR-derived products to support emergency management during volcanic crisis: La Palma case study

P. Ezquerro [a,*], G. Bru [a], I. Galindo [b], O. Monserrat [c], J.C. García-Davalillo [a], N. Sánchez [b], I. Montoya [b], R. Palamà [c], R.M. Mateos [a], R. Pérez-López [a], E. González-Alonso [d], R. Grandin [e], C. Guardiola-Albert [a], J. López-Vinielles [a], J.A. Fernández-Merodo [a], G. Herrera [a], M. Béjar-Pizarro [a]

[a] Instituto Geologico y Minero de España (IGME), CSIC. Geological Risk and Climate Change Department, 28003 Madrid, Spain
[b] Instituto Geologico y Minero de España (IGME), CSIC. Geological Risk and Climate Change Department, 35003 Las Palmas, Spain
[c] Remote Sensing Department, Geomatics Research Unit, Centre Tecnologic de Telecomunicacions de Catalunya, 08860 Castelldefels, Spain
[d] Instituto Geográfico Nacional, 28012 Madrid, Spain
[e] Université de Paris, Institut de physique du globe de Paris, CNRS, Paris, France

ARTICLE INFO

ABSTRACT

This paper analyses the performance of SAR-based results to support emergency management operations during the volcanic crisis of La Palma island. Tajogaite eruption began on September 19th 2021 affecting a high populated area and the surrounding farmland, used for different agricultural purposes. SAR datasets obtained from Sentinel-1, COSMO-SkyMED, PAZ-TerraSAR-X and Capella satellites, were processed to calculate amplitude, coherence and differential interferograms. These results have permitted to map the morphology of the volcanic cone, the evolution of lava flows and the regional displacements. The comparison of the results obtained with the different satellites has been useful to understand their performance during an emergency scenario triggered by a volcanic eruption. COSMO-SkyMED has provided the most useful information for the analysis of the cone morphology and the lava flows. Sentinel-1 showed the best performance for regional displacements monitoring, whereas PAZ results was the second best option for all the retrieved products.

1. Introduction

There are more than 1331 volcanoes with activity suspected or confirmed during the last 10,000 years on our planet (Volcanoes of the World 4.11.1 updated 18/08/22, Global Volcanism Program, 2013). Approximately 800 million people live around 100 km from a volcano in 86 countries (Loughlin et al., 2015). During the 20th century, volcanic hazards caused about 80,000 deaths (Sigurdsson et al., 2015) mostly related to a small number of eruptions demonstrating the potential for devastating mass casualties in a single event (Loughlin et al., 2015). Despite exponential population growth, the fatalities per eruption have decreased markedly in the past decades, suggesting that risk reduction measures such as monitoring, communication and early warning are efficient to a certain extent (Auker et al., 2013). Conversely, volcanic activity is associated with increasingly large economic impact. The resulting global economic loss from the modest-sized Eyjafjallajökull eruption in Iceland during 2010 amounted to about US$1.7 billion for the aviation industry alone (UNISDR, 2013), and it has been estimated to reach a total of US$5 billion including the effects on global businesses and supply chains (Ragona et al., 2011).

Eruptions range from violently explosive to gently effusive, from short lived (hours to days) to persistent over decades or centuries, from sustained to intermittent, and from steady to unsteady (Siebert et al., 2015).

For the eruptions affecting densely populated areas it is necessary to guarantee, during the emergency, the safety of the population, which

requires a precise and reliable monitoring of the evolution of the volcano and the associated geological hazards.

Implementing monitoring programs is therefore essential to provide civil authorities with useful and easy-to-understand data and products to analyze the evolution of volcanic hazards during the emergency and to make effective risk-based decisions.

Earth Observation data constitute a well suited source of information for this purpose, because they allow to remotely monitor the affected areas providing a good cost-effective spatial coverage. Specifically, active Synthetic Aperture Radar (SAR) sensors have the capability of operating night and day and seeing through meteorological cloud cover. SAR can also penetrate through relatively dense ash/aerosols plumes, which is a major asset to provide observations during the course of volcanic eruptions. The pixels of SAR images contain an amplitude and a phase component, both of which provide information relevant to volcano monitoring (Ebmeier et al., 2018). Typical SAR products derived from amplitude are SAR intensity images that reflect the scattering properties of the terrain surface, which allows mapping and characterizing volcanic structures and deposits, as well as measuring feature motion by pixel offset. Phase variations of SAR image pairs obtained with Interferometric SAR (InSAR) provide coherence products, surface deformation products and Digital Elevation Models (DEM). These products allow to characterize and monitor several processes in active and erupting (pre, co and post) volcanoes of different typologies, such as:

- Lava dome growth by analyzing backscattering changes (Ozawa and Kozono, 2013; Pallister et al., 2013; Plank et al., 2019; Saepuloh et al., 2015; Wadge et al., 2011; Wang et al., 2015), amplitude shadow (Arnold et al., 2017), amplitude pixel offset tracking (Mania et al., 2019; Shevchenko et al., 2021) and DEM generation by InSAR (Kubanek et al., 2015b).
- Crater morphology (Arnold et al., 2018; Walter et al., 2019) and opening/closing of effusive vents (Ruch et al., 2016) by means of backscattering changes.
- Volcanic edifice morphological changes: cone formation, growth and changes in shape by backscattering changes (Garvin et al., 2018; Plank et al., 2020), shadow, DEM.
- Cracks/fractures formation by backscattering changes (Hjartardóttir et al., 2016; Walter et al., 2015).
- Mapping of depositional features (such as ash or tephra) and flow structures (lava, lahars, and pyroclastic flows) by means of backscattering changes (Dualeh et al., 2021; Saepuloh et al., 2010) and interferometric coherence changes (Dietterich et al., 2012; Meyer et al., 2015; Wadge et al., 2002; Xu and Jónsson, 2014).
- Thickness of flow structures by means of amplitude shadow (Wadge et al., 2011, 2012) and DEMs from which the effusion rate can be derived (Albino et al., 2020; Arnold et al., 2017; Kubanek et al., 2015a, 2017; Poland, 2014).
- Ground deformation associated with different phenomena: intrusion of magmatic bodies at depth (Sigmundsson et al., 2010), dike intrusion (González et al., 2015; Montgomery-Brown et al., 2010; Sigmundsson et al., 2015), emptying of the magmatic chamber (deflation) (Baker and Amelung, 2012), cooling/contraction of lava flows (Lu et al., 2005; Wittmann et al., 2017), volcano flank stability (González et al., 2010; Schaefer et al., 2019), gravitational spreading (Lundgren et al., 2004), movement of faults/tectonic structures (Gudmundsson et al., 2016) and caldera subsidence (Shreve et al., 2019)

Nowadays there is a great amount of SAR data available from different satellite missions, with different image extent, spatial resolution, radar bands and revisit time, which determines their suitability to monitor the above mentioned phenomena. For instance, several works studying volcanic eruptions have used multi-sensor satellite monitoring to investigate different processes. Arnold et al. (2017) studied the extrusion rates at El Reventador Volcano in Ecuador, between 2011 and 2016, using X-band SAR data from TanDEM-X to calculate topographic changes and C-band data from RADARSAT-2 to retrieve lava flow extent (by exploiting backscattering changes) maps and lava flow thickness (by exploiting radar shadow). They also used RADARSAT amplitude data to study the dome and crater morphology and performed an interferometric analysis with the phase component to model the dyke intrusion. The 2011 Puyehue-Cordon Caulle eruption (Chile) was studied by Bignami et al. (2014), who applied SAR Interferometry using ENVISAT-ASAR data to study, on a monthly sampling basis, the deformation occurred just before the beginning of the eruption and the subsequent deflation. Moreover, the authors exploited COSMO- SkyMed high resolution amplitude imagery to map the extent of the lava flows. The work of Dumont et al. (2018) reviews the different SAR products delivered during the 2014–2015 Holuhraun Eruption in Iceland, which included InSAR-retrieved surface deformation maps derived from COSMO-SkyMed data, morphometric data obtained by using amplitude SAR images acquired by the TSX constellation, and thickness estimates of the lava field obtained by using DEMs derived from TanDEM-X data. In the work by Xu and Jónsson (2014), the 2007–2008 volcanic eruption on Jebel at Tair island (Red Sea) was analyzed with multisensor SAR interferometry. They mapped the lava areal extent and evolution with ALOS-1 interferometric coherence data (with limited time resolution due to the long revisit time of the satellite) and estimated the volume of the new lava flows by comparing pre-eruptive DEM generated with L-band data and post-eruptive DEM generated with TanDEM-X data. They studied the co-eruptive surface deformation and dyke modelling using ALOS-1, ERS and ENVISAT interferograms and additionally estimated the post-emplacement lava flow deformation due to cooling using ten consecutive ALOS interferograms with a chain stacking approach (Biggs et al., 2007). In general, TanDEM-X is better suited for DEM generation, whereas Sentinel-1 usually performs better when monitoring shallow intrusions of large areas with a high frequency and medium coherence loss, and high-resolution SAR data typically offer better performance for mapping morphological features.

However, although many studies devoted to the generation of these products from SAR data can be found in literature, there is a lack of studies focusing on the generation of these products for operational use in the event of an emergency, which should meet some particular requirements (e.g. quick availability of the satellite data, availability of experts to generate the needed products, which must further be easily understandable for the decision-making authorities, etc.). A particular need we found during La Palma 2021 emergency, was the development of a clear and straightforward method to help decide which data are best suited for each application (depending on different factors such as spatial resolution, revisit time, availability, etc.). A method based on the critical evaluation from a real experience would thus be of great value.

This paper addresses that need, providing a method together with a series of recommendations, based on the analysis of the SAR-based products generated by the IGME-InSARlab team during the 85 days of La Palma eruption, in support of the Special Plan for Civil Protection and Emergency Care for volcanic risk in the Autonomous Community of the Canary Islands (PEVOLCA) scientific committee. The IGME-InSARlab team worked during the 3 months of the eruption, providing SAR-based products to the scientific committee, formed by the following institutions: Instituto Geográfico Nacional (IGN), Centro Superior de Investigaciones Científicas (CSIC), Agencia Española de Meteorología (AEMET), Universidad de La Laguna, Universidad de Las Palmas de Gran Canaria, Instituto Volcanológico de Canarias (INVOLCAN), Instituto Geológico y Minero (IGME) and Instituto Español de Oceanografía (IEO).

This eruption, which affected densely populated areas of the island and lasted 85 days, caused more than 800 million euros in damages and the evacuation of more than 7000 people (Cabildo La Palma, 2022).

In this paper, we present 3 SAR-derived products that IGME team produced during La Palma emergency to identify potential geohazards

associated to the eruption. Specifically, the aims of these products were to monitor 1) the evolution of the morphology of the volcanic edifice; 2) the extension of lava flows and 3) the surface ground deformation. We then evaluate the performance/operativity of the 5 different SAR dataset that we used for emergency support (Capella, COSMO-SkyMed -Spotlight, COSMO-SkyMed -Stripmap, PAZ and Sentinel-1), considering both technical and accessibility factors.

2. La Palma background

2.1. Geological setting

The island of La Palma is located in the western part of the Canary Islands, a group of seven main intraplate volcanic islands 100 km off the NW African continental shelf. This volcanic island (Fig. 1) rises over a Pliocene (4.0–3.0 Ma, Camacho et al., 2009) intrusive basal complex (Klügel et al., 1999; Staudigel et al., 1986), which outcrops in the lower

areas of the Caldera de Taburiente. The next stage in the evolution of the island is the development of the Northern shield beginning with the Garafía and Lower Taburiente volcanoes (1.72–1.2 Ma, González et al., 2010), overlapped by Upper Taburiente volcano (1.08–0.44 Ma, González et al., 2010), Cumbre Nueva Series (1–0.7 Ma; Klügel et al., 1999) and Bejenado edifice (0.71–0.65 Ma; Klügel et al., 1999). Current volcanic activity is related to the last phase of the island and to a magmatic migration towards South that began in the Upper Taburiente area (Carracedo et al., 2001) and formed the Cumbre Vieja volcano around 0.7 Ma ago (Klügel et al., 1999). The resulting formation, known as Cumbre Vieja Series ridge, overlaps part of Cumbre Nueva Series and is described as a volcanic rift zone with a north–south alignment of vents, fissures and faults (Carracedo, 1994). This area has been affected by eight volcanic eruptions within the historic period, lasting between 24 and 85 days, in 1430/1440, 1585, 1646, 1677, 1712, 1949, 1971 and 2021 (Klügel et al., 1999), the latter being the longest. One of the main geological processes that configured the island topography over its last
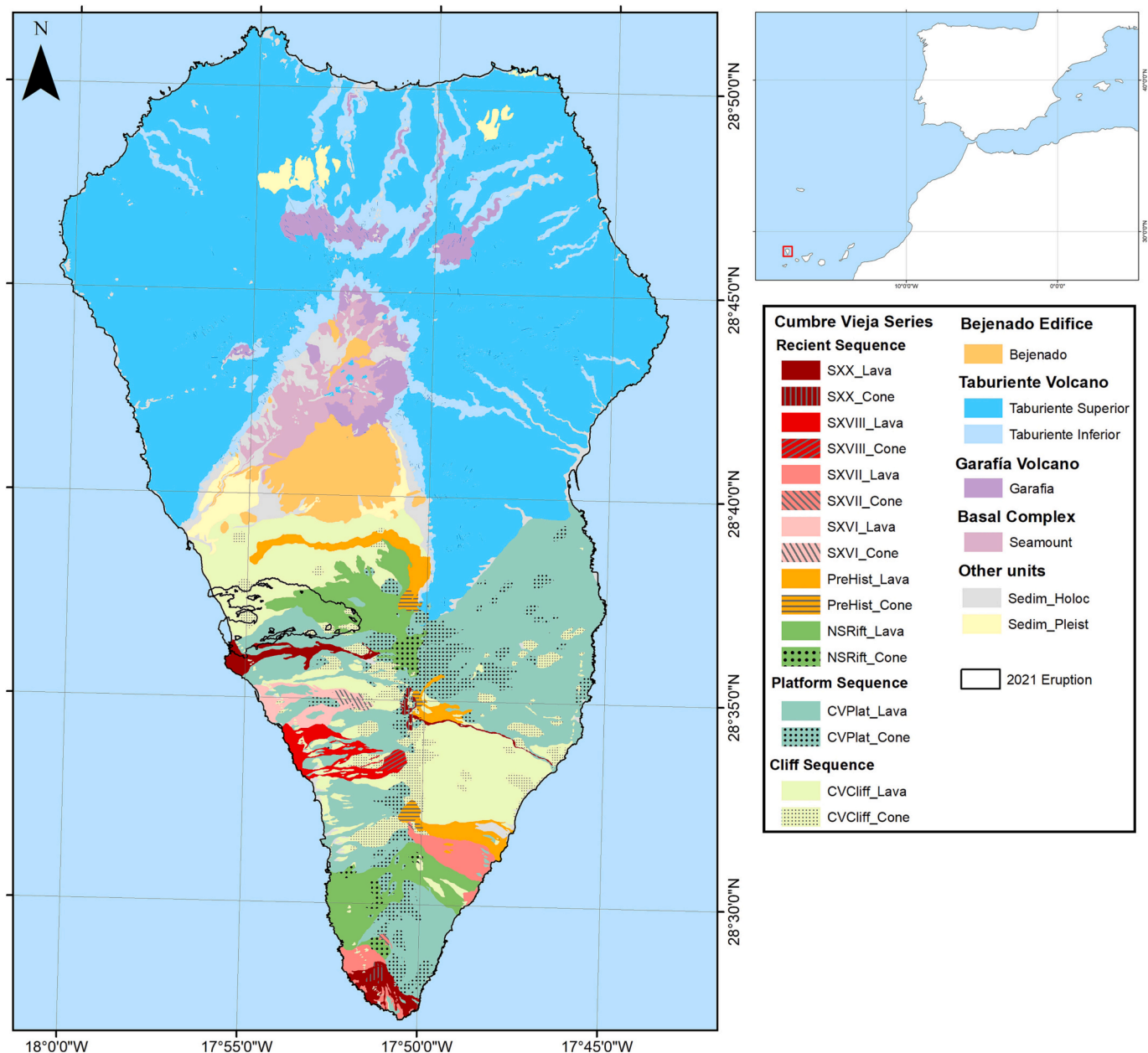
Fig. 1. Geological map of the island of La Palma based on the IGME GEODE map (Bellido Mulas et al., 2023). Cumbre Vieja Series are divided into sequences and historical eruptions subdivided by century. The black polygon limits the area covered by the 2021 eruption cinder cone and lavas.

development stages, relates to the massive collapses documented for the different volcano edifices. Garafía or Lower Taburiente volcanoes, depending on the authors (Carracedo et al., 2001; Masson et al., 2002), suffered a major collapse (1.72–0.8 Ma) probably related to the "Playa de La Veta" submarine deposits (Masson et al., 2002; González et al., 2010). The landslide scars associated with these collapses were partially covered by Upper Taburiente and Cumbre Nueva deposits. Subsequently, around 0.5 Ma, a second collapse occurred, which generated a visible scar in Cumbre Nueva ridge, defined the present geomorphic configuration of Los Llanos de Aridane valley and produced a large submarine debris avalanche (Camacho et al., 2009; González et al., 2010; Masson et al., 2002).

Cumbre Vieja volcano was first described as a singular north-south rift overgrowth from Cumbre Nueva (Afonso, 1974; Ancoechea et al., 1994). Yet later works suggest the existence of other two minor rifts in NE and NW directions (Carracedo, 1994). The activity of those rifts allowed Day et al. (1999) to define three sequences. The oldest one (cliff-forming sequence, 125–20 ka) was characterized by an evenly distributed activity of all the rift areas that formed most of the present Cumbre Vieja edifice. The platform-forming sequence (20–7 ka) suffered a displacement of the activity of the north-east rift that resulted in a great increment of the eastern platform. North-south rift remained at the same activity level, whereas north-west rift quickly decreased its activity during this period. Sub-historic and historic sequence (< 7 ka) reveals a cessation of the north-east rift activity, further indicating that eruptive

processes mainly concentrated in the axial part of the north-south rift. The vents during this period present two main alignments: near north-south and west-northwest.

2.2. The 2021 volcanic eruption in the island of La Palma

The 2021 eruption, recently named as "Tajogaite", but also referred as "Cumbre Vieja" or "Cabeza de Vaca" eruption, began on Sunday September 19th and lasted until December 13th, after 85 days of near-uninterrupted emission of lava flows and pyroclastics. Seismic activity during the September–December period, recorded by the National Geographical Institute (IGN), amounted 9186 events, from which more than 2400 exhibited magnitudes (mgLb) over 3.0, and 7 over 5.0. The maximum observed macroseismic intensity was IV-V (EMS98).

In the morning of September 19th several earthquakes reaching magnitude 3.8 at shallow depths, accompanied by subterranean noises, alerted about the possibility of an imminent eruption. First vents opened near and inside an old eroded cone in the "Cabeza de Vaca" area, at a distance of around 1 km NE from the "Montaña Rajada" old cone and SE "El Paraiso" neighborhood (Fig. 2). The fissure nature of the eruption generated several vents discharging pyroclastics and lava flows that covered more than 100 ha during the first hours affecting around 160 structures (Copernicus EMS, 2022). Main vents were located 5.7 km inland and the lava flows lasted ten days to reach the coastline on September 29th, generating a new lava delta and vigorous gases
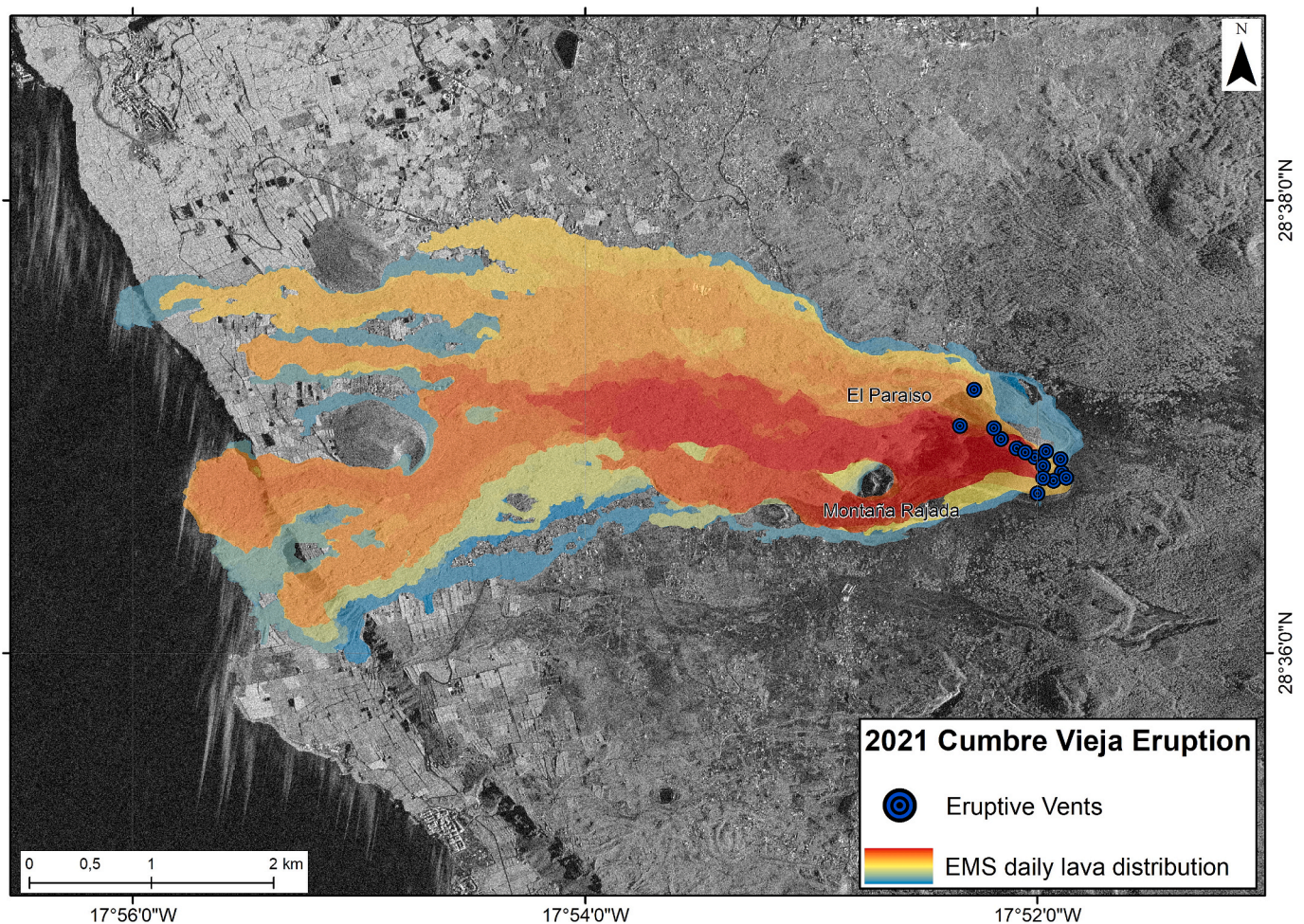
Fig. 2. Evolution of the lava flows during 2021 Tajogaite Eruption. The color of the lavas shows their position from 19-Sept (Red) to 17-Dic (Blue) based on Copernicus EMS Grading products (EMSR546 activation) obtained using COSMO-SkyMed and Pleiades images. Vents location is based on Copernicus EMS. Base image generated using the 24/12/2021 PAZ Descending image. (For interpretation of the references to color in this figure legend, the reader is referred to the web version of this article.)

emission at the lava-seawater interface. The new formed cone reached more than 1071 m a.s.l. in altitude and 700 m in diameter at the base, with an estimated volume of 36 Mm³ (Civico et al., 2022). Lava flows covered 1218.87 ha affecting the villages of Los Llanos de Aridane, El Paso y Tazacorte with near 1676 buildings damaged and 370.07 ha of banana trees (228.69 ha), avocado trees (27.43 ha) and vineyards (68.05 ha) affected (Cabildo La Palma, 2022). 2329 people lived in houses affected by the lava flows and more than 7000 people were evacuated during the emergency (Cabildo La Palma, 2022). Direct losses are valued in more than 230 M€ (Consorcio de Compensación de Seguros, 2022).

3. Materials and methods

3.1. SAR data and validation data

During the Tajogaite eruption the IGME team used images from four different SAR constellations: Sentinel 1 A/B (S-1), PAZ-TerraSAR-X (PAZ-TSX), COSMO-SkyMed (CSK) and Capella. The different platforms allow to perform different analysis adapted to the best combination of resolution, revisiting time and wavelength available.

S-1 is a constellation of two satellites developed by the European Space Agency (ESA) that provide C-band SAR images of medium-high resolution (5 × 20 m), wide sensing area (250 km width) and a repeating cycle of 6 days (Torres et al., 2012). During the eruption period (September – December 2021), 25 images in ascending and 25 in descending trajectory were acquired (Fig. 3), meaning one acquisition each 6 days per trajectory (Table 1). They were freely available to download at the Copernicus Open Access Hub two hours after each acquisition. S-1 images allow to generate regular and consistent interferometric products constituting the core of remote sensing emergency support activity, especially for fast assessment and surface deformation monitoring.

X-band constellations mount very high-resolution radar sensors (from 3 to 0.5 m) specialized on urban environment monitoring and commercial projects (Castelletti et al., 2021; Covello et al., 2010; González et al., 2011; Werninghaus and Buckreuss, 2009). During special events like natural disasters, they are also used for emergency tasks and even re-programed to increase the repeating cycle and operate at advanced acquisition modes.

PAZ satellite is one of the most recent SAR satellites launched by European space agencies. It is operated by HISDESAT in cooperation with the Spanish Aerospace Institute (INTA) and fully compatible with

Table 1
Sentinel-1 Interferogram list. Red square marks the co-eruptive interferograms.

Ascending		Descending	
Start Date	End Date	Start Date	End Date
27/08/2021	02/09/2021	29/08/2021	04/09/2021
02/09/2021	08/09/2021	04/09/2021	10/09/2021
08/09/2021	14/09/2021	10/09/2021	16/09/2021
14/09/2021	20/09/2021	16/09/2021	22/09/2021
20/09/2021	26/09/2021	22/09/2021	28/09/2021
26/09/2021	02/10/2021	28/09/2021	04/10/2021
02/10/2021	08/10/2021	04/10/2021	10/10/2021
08/10/2021	14/10/2021	10/10/2021	16/10/2021
14/10/2021	20/10/2021	16/10/2021	22/10/2021
20/10/2021	26/10/2021	22/10/2021	28/10/2021
26/10/2021	01/11/2021	28/10/2021	03/11/2021
01/11/2021	07/11/2021	03/11/2021	09/11/2021
07/11/2021	13/11/2021	09/11/2021	15/11/2021
13/11/2021	19/11/2021	15/11/2021	21/11/2021
19/11/2021	25/11/2021	21/11/2021	27/11/2021
25/11/2021	01/12/2021	27/11/2021	03/12/2021
01/12/2021	07/12/2021	03/12/2021	09/12/2021
07/12/2021	13/12/2021	09/12/2021	15/12/2021
13/12/2021	19/12/2021	15/12/2021	21/12/2021
19/12/2021	31/12/2021	21/12/2021	27/12/2021

the Germany Space Agency (DLR) SAR constellation TerraSAR-X. During Tajogaite eruption the PAZ acquisition rate over the area was increased including three different tracks in ascending and descending trajectories. All the trajectories provide a 11-day revisit time (González et al., 2011). This frequency was complemented during the first month with TSX compatible acquisitions (Alonso-González et al., 2021). PAZ-TSX images are suited to generate interferometric products, but due to temporal decorrelation the most important contribution was the amplitude images and Multi-Temporal Coherence maps. A total of 71 PAZ and 10 TSX were supplied during the entire crisis (Fig. 3).

Another source of X-band imagery was the CSK constellation (Covello et al., 2010). Italian Space Agency satellites contribution was requested by Copernicus Emergency Management Service to elaborate the near-daily grading map. Acquisitions in Stripmap (3 m resolution) and Spotlight (1 m resolution) modes with a 1 to 4 days repeating cycle and 5 tracks (3 Ascending, 2 Descending) provided daily information about the lava flows location and cone morphology. Focusing on the
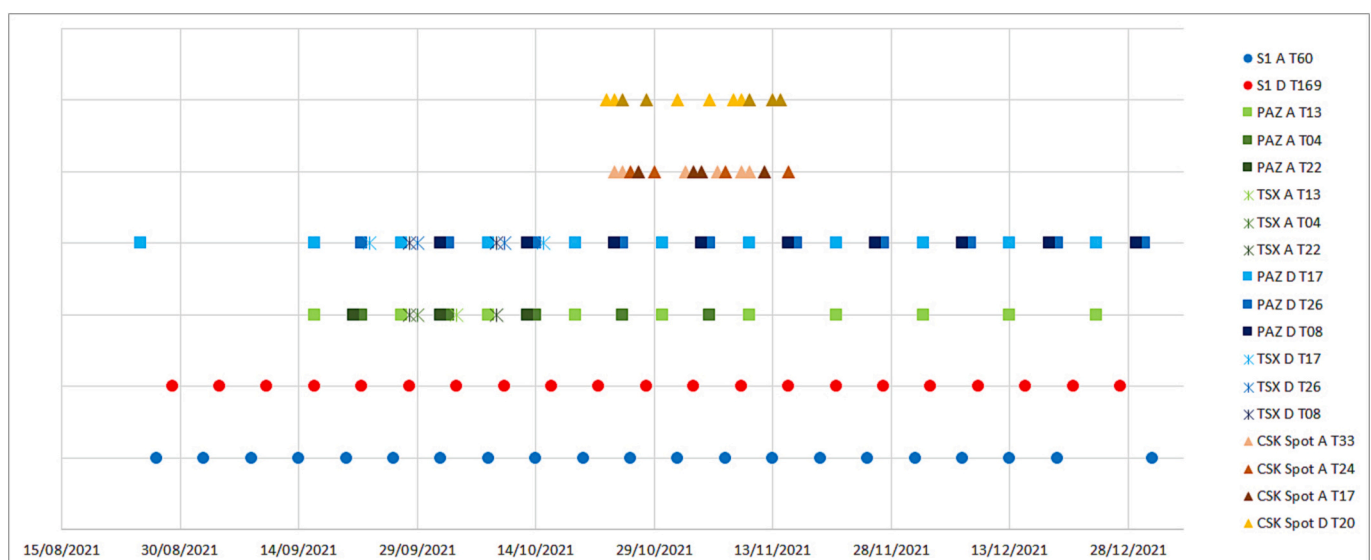
Fig. 3. Temporal distribution of SAR Images for La Palma depending on the Satellite constellation: S-1 (Dot), PAZ (Square), TSX (Cross) and CSK (Triangle).

Spotlight mode, 25 images were served covering a period of one month of the emergency (Fig. 3).

Last, Capella Space SAR private company also provided valuable information for emergency management through some ultra-high resolution X-band images (0.5 m) (Castelletti et al., 2021). The first satellite of the constellation was launched in August 2020, meaning that this eruption was one of the first covered by Capella system. Still scarce, this information is very useful for early detection of cone features and lava flow anomalies. The lack of continuity in the acquisition orbits prevent from advanced interferometric products. This constraint is a consequence of the "agility" of the satellites, which is a technical requirement to achieve sub-daily revisit capability of any target at the Earth surface. Six Capella images were available.

Validation of the products generated during the emergency was accomplish using in-situ displacement monitoring systems (i.e. GNSS Permanent stations, GNSS or levelling networks, extensometers and tiltmeters), volcanic products maps (lava flows and ashes) and direct observation monitoring (i.e. UAV images, field observations, measurement of ash thickness). Whereas in-situ systems are designed as early warning systems, they are also valuable for validation of the interferometric products. The relatively new growth of Unmanned Aerial Vehicles (UAV) improved the active volcano surveillance with detailed optic and thermic data (Wakeford et al., 2019), also providing the possibility to calculate digital elevation models (DEMs) of cones and lava flows (De Beni et al., 2019; Civico et al., 2022; Nakano et al., 2014), and allowing the validation of Amplitude and Multi-Temporal Coherence products. During the eruption, 10 GNSS permanent stations and 4 tiltmeters were active providing sub-daily data. GNSS data were processed, analyzed and served by the IGN, responsible in Spain for volcanic monitoring (IGN, 2022b). Additionally, a continuous ash thickness measurement campaign was carried on and several optical and thermic UAV flights were performed daily.

3.2. SAR products

3.2.1. SAR amplitude

SAR Amplitude images contains the information concerning the intensity of the radiation backscattered by the different surfaces towards the satellite (Ferretti et al., 2007). Multiple parameters have a significant influence on the radar backscatter intensity, depending both on the sensor acquisition specifications (radar band, incidence angle, polarization, spatial resolution and orbit) and on the illuminated surface composition (surface terrain roughness, topography, water content and dielectric properties). In general, mirrored back-radiation will have higher values over artificial surfaces (double bounce at buildings), slopes facing the radar antenna (sum of backscattering responses or foreshortening) or bare soil (surface roughness) than a dry, flat and smooth area. Several studies have tracked different volcanic process involving morphological and roughness changes that modify the backscatter amplitude of SAR images. The processes include dome growth (Ozawa and Kozono, 2013; Pallister et al., 2013; Plank et al., 2019; Saepuloh et al., 2015; Wadge et al., 2011; Wang et al., 2015), crater morphology (Arnold et al., 2018; Walter et al., 2019), flow structures (lava, lahars, and pyroclastic flows) emplacement (Bignami et al., 2014; Di Traglia et al., 2018; Dualeh et al., 2021; Saepuloh et al., 2010; Terunuma et al., 2005; Weissel et al., 2004), lava flow heights from radar shadow (Arnold et al., 2017; Wadge et al., 2012), ash emplacement (Arnold et al., 2018) and shallow landslides in the volcanic edifice (Ebmeier et al., 2014). The methodologies vary from the visual examination of single images, to backscattering change detection from multiple images. Another method using SAR amplitude images is the pixel offset tracking for investigating large-scale (meter-level) deformations, applicable in dome growth (Mania et al., 2019; Shevchenko et al., 2021). In the work of Dualeh et al. (2021) a summary of case studies classified by the type of eruption, studied process and method is presented.

SAR visual analyses of amplitude data are independent of the satellite revisiting period and data can be directly compared with that from other satellites or UAV. Changes in the features and backscattering generated by the different acquisition geometries and incidence angles must be considered during the analysis of the results. During La Palma eruption four datasets from different satellites were available, all of them with capacity to perform an amplitude analysis. Images from Sentinel-1, CSK and PAZ were processed using ESA SNAP software (Veci et al., 2014) applying the processing chain shown in Fig. 4. Images were first calibrated and filtered to facilitate comparison and reduce speckle effects. Then, they were geocoded and transformed into dB values using a decimal logarithmic expression but avoiding multilooking to maintain the highest resolution. All the available CSK and PAZ images were processed to generate SAR amplitude products while S-1 data were early discarded for this analysis mainly due to the lower spatial resolution.

The purpose of SAR amplitude images during the emergency was the monitoring of the cone morphology and early detecting features that could lead to collapses of the volcanic edifice. Slopes facing towards or away from the sensing direction appear in radar images as foreshortened (bright areas) or lengthened (dark areas) respectively. The effects of layover and shadow allow to detect cliffs and lava flow channels. Changes in the position of these features is useful to understand the eruption dynamic and detect structural anomalies.

3.2.2. SAR coherence: multi-temporal coherence (MTC) maps

One of the products obtained from an interferometric pair of SAR images is the coherence map. Coherence of the scene is the absolute value of the local coherence, cross-correlation coefficient of the SAR image pair estimated over a small window (Ferretti et al., 2007). High coherence values indicate areas that generates a stable response in terms of phase. Coherence decreases when surfaces response varies between two acquisitions, such as the leave motion of dense tree areas, crop fields, water surfaces, fast moving areas (fast floods, sinkholes, rockfalls), etc. Coherence change detection maps are used in volcano eruption monitoring to identify melting of snow and ice near the crater (potential pre-eruptive sign) and map depositional features such as ash or tephra (Jung et al., 2016) as well as flow structures (lava, lahars, and pyroclastic flows) (McAlpin and Meyer, 2013; Meyer et al., 2015; Zebker et al., 1996).

Coherence and interferograms images were obtained using the interferogram generation workflow (Fig. 5) of ESA SNAP software (Veci et al., 2014). Coregistration of the SAR images pair was followed by the interferogram generation and the elimination of the topographic phase contribution. In order to preserve the maximum resolution available, multilooking has not been applied to obtain MTC results. Once geocoded, the coherence image is combined with the amplitude image of the second date and the amplitude image of the first date into a false color RGB image (MTC map) (Boccardo et al., 2015) with the red, green and blue channels assigned respectively (Fig. 5).

MTC maps are useful to monitor volcanic mass flows such as lava, pyroclastic density currents, and lahars (Poland, 2022). Changes in the lava flows and their activity can be tracked for the time periods between the image acquisition dates. These maps show different behaviors depending on the values of the three layers that compose it and can be studied to understand the processes of the area. The colors resulting from the combination represent a change in the soil characteristics that can be widespread, but the meaning must be analyzed locally. In the case of the island of La Palma, six main tones were defined (Fig. 6). Light red areas present pixels with high coherence (R) and medium values of amplitude (G&B) represent natural bare areas, old lava flows and lavas from the ongoing eruption but not active during the MTC time span. Bright green-blue areas are mainly greenhouses with medium-low coherence but very high amplitude. Near white pixels with the highest values of the three layers characterize the best scatterers, including urbanized areas and structures. Green areas are detected when new lava flows (Medium amplitude in date 2 image) with low coherence cover areas with low amplitude in the date 1 image like the sea or very active
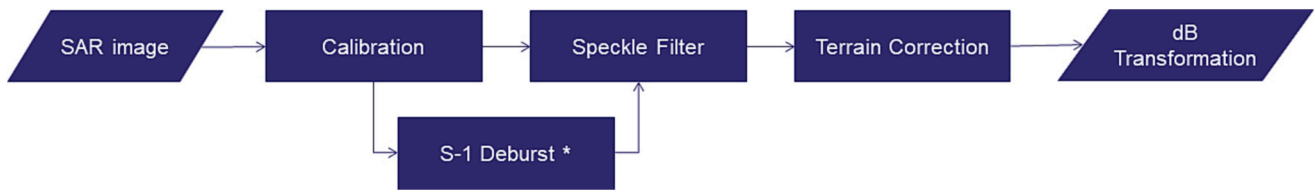
Fig. 4. Workflow for the generation of SAR amplitude images. *S-1 Deburst is only performed when using S-1 images.
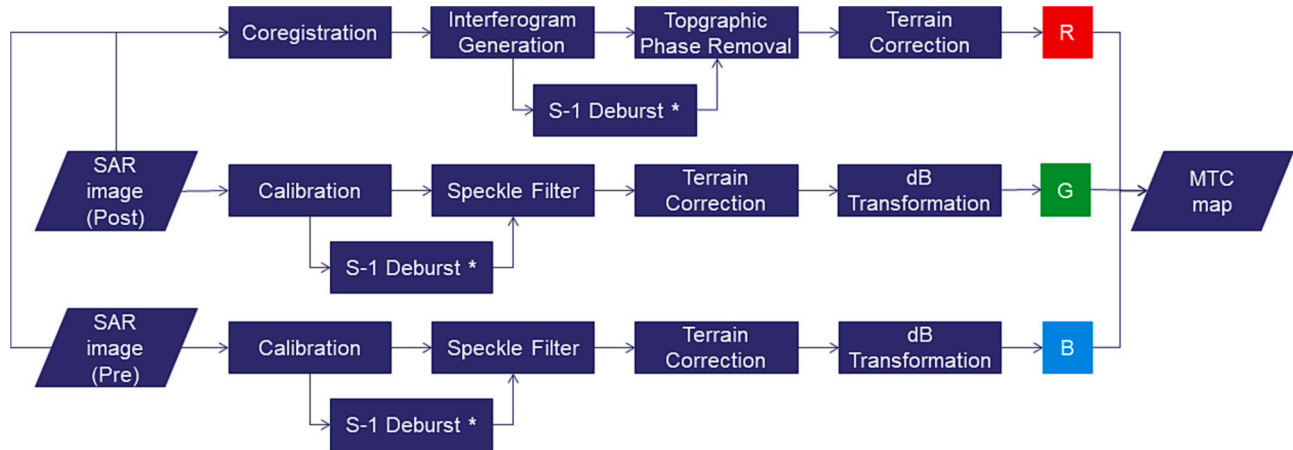

Fig. 5. Workflow for the generation of MTC maps. *S-1 Deburst is only performed when using S-1 images. SNAP S-1 Coregistration includes TOPSAR Split, Apply Orbit, Back Geocoding and Enhanced Spectral Diversity.

lava channels of date 1. Blue areas represent the opposite case, new lavas over medium-high amplitude areas of date 1, for example new lavas covering greenhouses or very active lava channels of date 2. Last, dark green-blue areas are those with low coherence but medium amplitude. They are associated to active lavas in both dates.

Coherence is highly dependent on the time gap between both images, especially in a rapid-changing area like this. MTCs with long gaps between images allow to estimate new areas affected by lava flows, but lack to determine the activity of fresh lavas over previous lava flows from the same eruptive event. Short gaps achieve to obtain high coherence results over the inactive lava flows differentiating them from active ones. First type was generated using the PAZ eleven days revisiting data during all the eruption period and second one with the CSK spotlight and stripmap images (1, 3 or 4 revisiting time) when interferometrically compatible.

3.2.3. SAR interferometry

Surface deformation was measured using interferograms, processed by SNAP software (Veci et al., 2014; Fig. 7). First, two SAR single look complex (SLC) images were coregistered to align them and the interferometric products generated (interferogram and coherence map). In the case of Sentinel-1 data, debursting was applied at this stage. Topographical phase contribution was removed using SRTM DEM. At that point, the application of multilooking to reduce the signal noise ratio was considered adjusting a 2×9 looks for Sentinel and 3×3 looks for PAZ and CSK stripmap products (final square pixel around 30 and 4.5 m respectively). Last, interferograms were processed in two modes, one unfiltered for detailed analysis and the other applying a Goldstein filtering (Goldstein and Werner, 1998) for fast interpretation during the emergency cycle. Unwrapping of the obtained interferograms was not considered regarding the large atmospheric effects detected in the area, mainly related to the steep orography (González et al., 2010).
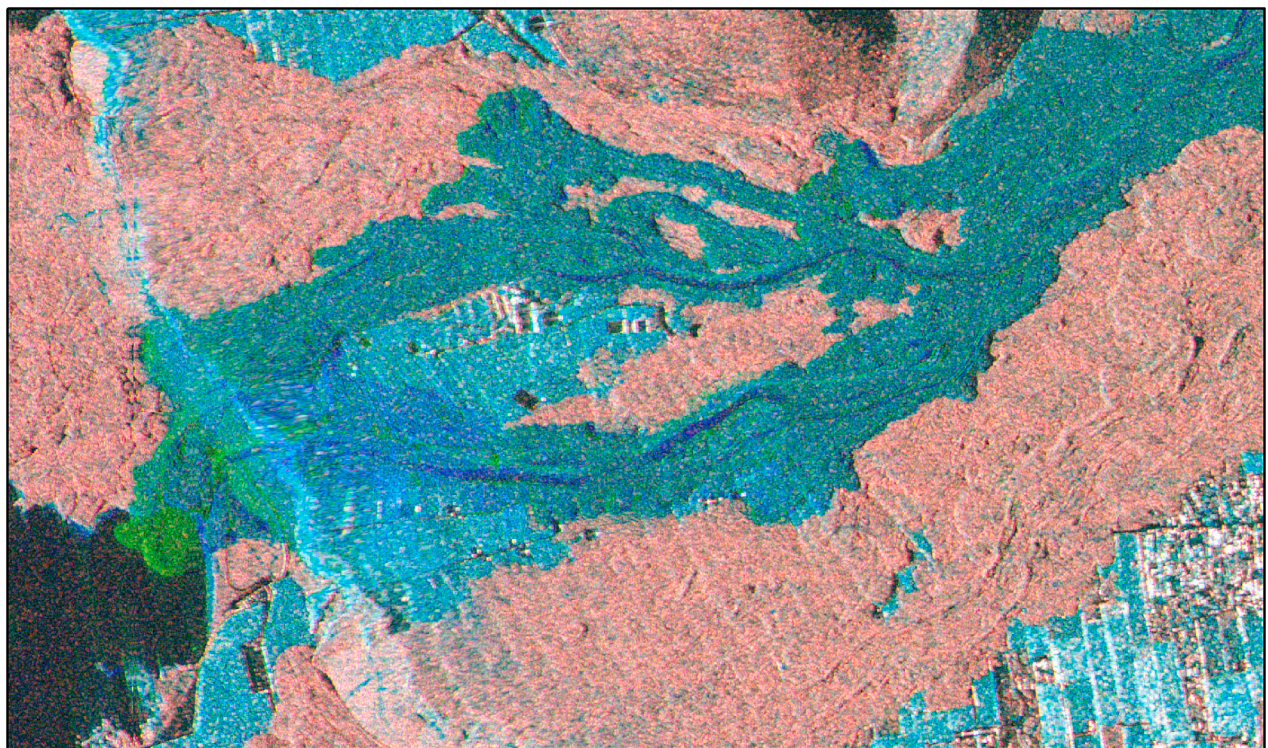
During the volcanic event 40 interferograms were systematically computed after image reception using ascending and descending Sentinel-1 data including pre and post-event monitoring. Additional PAZ and CSK interferograms were calculated for in-detail measurement of co-eruptive pair and supporting analysis of anomalies detected by Sentinel-1 and field researchers.

Interferograms provide information about the surface displacement evolution during the event, focusing on the regional size, detecting changes in the intrusion of magmatic bodies, propagation of dikes or emptying of the magmatic chamber (Valerio et al., 2022; Xu et al., 2020). Also local displacements related to the cooling and contraction of lava flows can be detected and analyzed (Wittmann et al., 2017).

Displacements retrieved from an interferometric processing can be affected by different sources of noise and decorrelation (temporal and geometric decorrelation, volume scattering, atmospheric effects and processing errors). The accuracy estimating those displacements can be improved by processing large stacks of SAR images using Multi-Temporal InSAR (MT-InSAR) techniques (Berardino et al., 2002; Ferretti et al., 2001; Hooper, 2008). Those techniques target pixels whose scattering properties remain consistent in time and in order to calculate the displacements associated with the area covered by each selected pixel (Permanent scatterers or Distributed scatterers; Berardino et al., 2002; Ferretti et al., 2001).

After La Palma eruption two different MT-InSAR approaches were performed with the tools provided by the Geohazards Exploitation Platform (GEP), which is part of the Thematic Exploitation Platforms (TEP) virtual work environments initiative from the ESA. SAR data, processors and computational resources are provided through one coherent interface, allowing users to perform fast and straightforward SAR processes to produce surface deformation mean velocity maps and time series in an unsupervised manner. Using this environment simplifies the InSAR process because all the technical resources are external and SAR images and algorithms are located together. The platform allows SAR Big Data processing in a very fast way compared to local processing, which is very convenient to use in emergency response. However, GEP tools are semi-automatic and unsupervised, so it is convenient to validate the results or, at least, compare them with other data. To obtain two datasets for cross-comparison, we used the
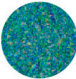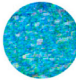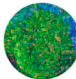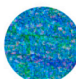
Fig. 6. Explanation of the RGB behaviors observed during La Palma eruption in the MTC maps.

Fig. 7. Workflow for the generation of interferograms.

processors P-SBAS and SNAPPING. Multitemporal InSAR results were obtained at the end of the eruption, but these tools can be helpful also during the emergency to retrieve mean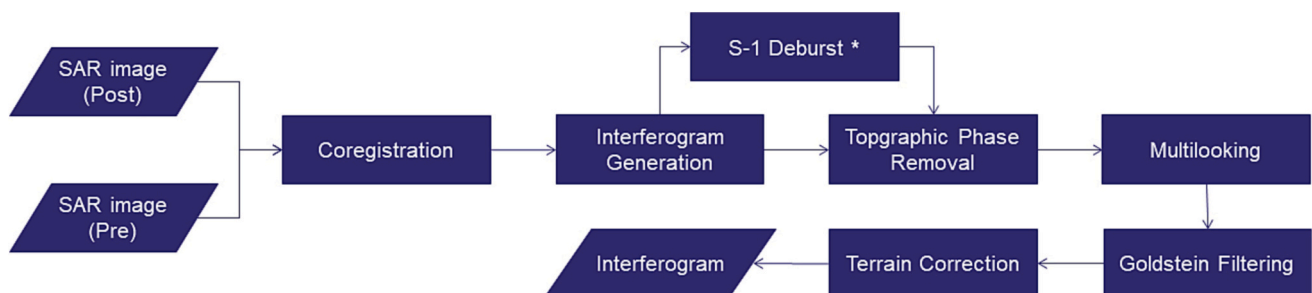 velocity results (where atmospheric and other nuisance artifacts are mitigated) in a fast way. Moreover, SNAPPING offers the possibility of easily adding newer SAR images to the multitemporal InSAR processing as it uses a Single Reference approach. P-SBAS processing chain provides a parallel computing solution (Casu et al., 2014; Manunta et al., 2019) for the SBAS approach (Berardino et al., 2002) and it was developed to handle massive SAR archives from current satellites. SBAS uses small baselines to limit the spatial decorrelation, multilooks data to reduce phase noise and applies a coherence-based pixel selection criterion. The multilook applied is 5×20 (azimuth x range) which generates pixels in the size of about 90×90 m. This tool was integrated into GEP by CNR-IREA (De Luca et al., 2015). SNAPPING is a solution, added to GEP by the Aristotle University of Thessaloniki (AUTh), the research group Microgeodesia Jaén (MJaen) and Terradue s.r.l., that combines the capabilities of SNAP (Veci et al., 2014) to generate the interferogram stack and StaMPS

(Hooper et al., 2012) to generate mean velocity maps and time series. SNAPPING uses a Single Reference interferometric processing approach compatible with StaMPS PSI methodology, an amplitude dispersion criterion for initial pixel selection and the option to apply atmospheric filters (Foumelis et al., 2018, 2021). We used the medium resolution SNAPPING service version, where PS point measurement represent the average motion of the surrounding 100 × 100 m area. First processing using P-SBAS includes 289 Sentinel-1 images from January 2017 to January 2022 in descendig adquisition geometry. Selected coherence as threshold for pixel selection was set in 0.8. SNAPPING processing cover the period from July 2019 to December 2021 with 133 Sentinel-1 images from the same track (169) and geometry (descending). A 0.4 amplitude dispersion threshold was considered for this processing and the atmospheric filtering was not applied in order to detect the pre-eruptive high motion gradient. PS-InSAR processing parameters are summarized in Table 2.

4. Results

4.1. Cone morphology

Continuous monitoring of the cone morphology evolution during a volcanic event is crucial for early detection and follow up of possible instabilities. Amplitude images derived from single SAR acquisitions are the main source of data for such recognition, but other information associated to the lava flows, like their approximated thickness, can also be estimated (Arnold et al., 2017; Wadge et al., 2012). High potential of this products for volcanic emergency management is related to the low influence of the cloud cover and ashes plume on the results, providing regular data of the cone. It should be considered that these images are not acquired in a zenithal view and show deformed features especially over steep slopes. The orbit acquisition geometry generates additional differences.

The main application in La Palma eruption was the visual recognition of the cone new features and evolution, covered by four different satellites (Capella, CSK, PAZ and Sentinel-1) with two acquisition geometries (except for Capella) and different modes (CSK Spotlight and Stripmap). This diversity of data allowed to compare their usefulness to analyze the cone evolution.

PAZ data provided 71 Stripmap images with a period of 11 days in 6 different tracks. The high resolution of those data (3 m pixel) allowed to monitor the evolution of the cone during the whole eruption and represented the main reference data to describe the cone morphological evolution (Fig. 8).

Fig. 8a show the first image of the cone after the beginning of the event (27/09/2021). Although the eruption started at the SE of the image, the eruptive fissure propagated towards the NW where the activity was focus. Thus, after nine days of eruption, a massive cone was already visible with at least two major vents and lava flows moving towards NW. The darkest area of the cone indicates an area of low

reflectivity probably related to the volcanic activity and radar beam direction, from SW to NE. One month later (Fig. 8b, 30/10/2021) the cone is better defined in an extension that remains near stable until the end of the eruption. The main crater is formed in the upper part, with three dominant strombolian behavior vents and an effusive vent in the NW mountainside. The crater rim of a previous volcano, observed on the SE of the Fig. 8a was clearly disrupted during the eruption due to a phreatic explosion that destroyed part of the older cinder cone, showing new sharp features in the radar images. The eruptive fissure evolved with narrow displacements of the vents along the fissure trend maintaining the effusive vent in the lower NW part, that still issue lavas to the north. Along the cone summit, the two vents on the NW seam to form a single bigger crater. To the SE, the main crater widens and two more vents appear (Fig. 8c, 21/11/2021). The last image, after the end of the eruption in December (24/12/2021), shows the opening of a new vent in the NE volcano flank that issued an important lava flow towards NW. New lava channels were clearly visible in this image (Fig. 8d). On the main cone, a wider central crater is observed, formed during the final phreatic explosions of the last eruptive phases. At the southeastern flank of the cone a small elongated depression detected trending NE-SW is related with the formation of a graben structure. On the same area, a new lava flow is detected towards SW.

CSK images covered the time period from 23rd October to 15th November. Twenty-five images from Spotlight mode provided very high-resolution data (1 m pixel) improving the morphological changes recognition. Fig. 9 shows the comparison between PAZ and CSK images acquired at the same time in both different orbit directions. Thanks to the finer resolution of CSK, the vents location and position of the slopes and cliffs could be more clearly identified and characterized with visual inspection. Also, possible anomalies or instabilities could have been early detected. Information provided by UAV images was highly enhanced using SAR information since first have severe difficulties during the most active periods (Fig. 9e).

Data from Capella constellation provided the highest resolution (less than 0.5 m pixel) with the possibility to define cone and lava flow features (Fig. 17a). However, its orbit changes still reduce their operability during emergencies. On the opposite side, Sentinel-1 data is the most stable and fast-responsive data, but the medium resolution (15 m pixel) of the Interferometric Wideswath (IW) mode decrease the usefulness of this data for morphological analysis (Fig. 17d).

During the emergency the SAR amplitude images represented an important complementary source of information, as they were obtained at any weather conditions, overpassing the volcanic plume, and some were acquired during the night, when other options like UAV were unavailable. Once processed, they were analyzed to detect new features in the cone area that could reveal changes of its morphology. This objective was achieved mainly using the high-resolution data from Capella and CSK Spotlight but also CSK and PAZ Stripmap mode. Anomalies detected were communicated to the IGME field team to monitor the area and confirm or dismiss them. Also, anomalies detected in-situ were considered by the remote sensing team and analyzed in the amplitude images.

4.2. Lava flow detection

Fast delineation of lava flows over large areas helps to optimize emergency services, as inhabitants evacuation, and reduce the possible damages. Monitoring of fresh lavas over older ones provide data about flow direction and possible spills over unaffected areas. Limiting their use, SAR images for MTC must be interferometric pairs, reducing the data availability.

During the first stage of the eruption the event was covered by PAZ images with a temporal difference of 11 days. MTC results shows in blue and green the greatest changes between the two images compared. Fig. 10a shows the initial changes with the appearance of the main cone and lava flows. It is important to highlight that the changes on the

Table 2
PS-InSAR processing parameters.

|	P-SBAS	SNAPPING
Orbit mode	Descending	
Track	169	
Mean incidence angle	0.66	
Initial date	16/01/2017	29/06/2019
End date	20/01/2022	21/12/2021
Number of SAR images	289	133
Thresholds for MP selection	0.80	0.40
Number of detected MP	49,564*	31,405
MP density [per km^2]	70	44.36
Pixel size [meters]	90 × 90	100 × 100
LOS velocity range [cm/year]	1.85 to −1.40	2.64 to −1.96
LOS velocity standard deviation	0.33	0.53
Max. total LOS displacement [cm]	19.19	18.72
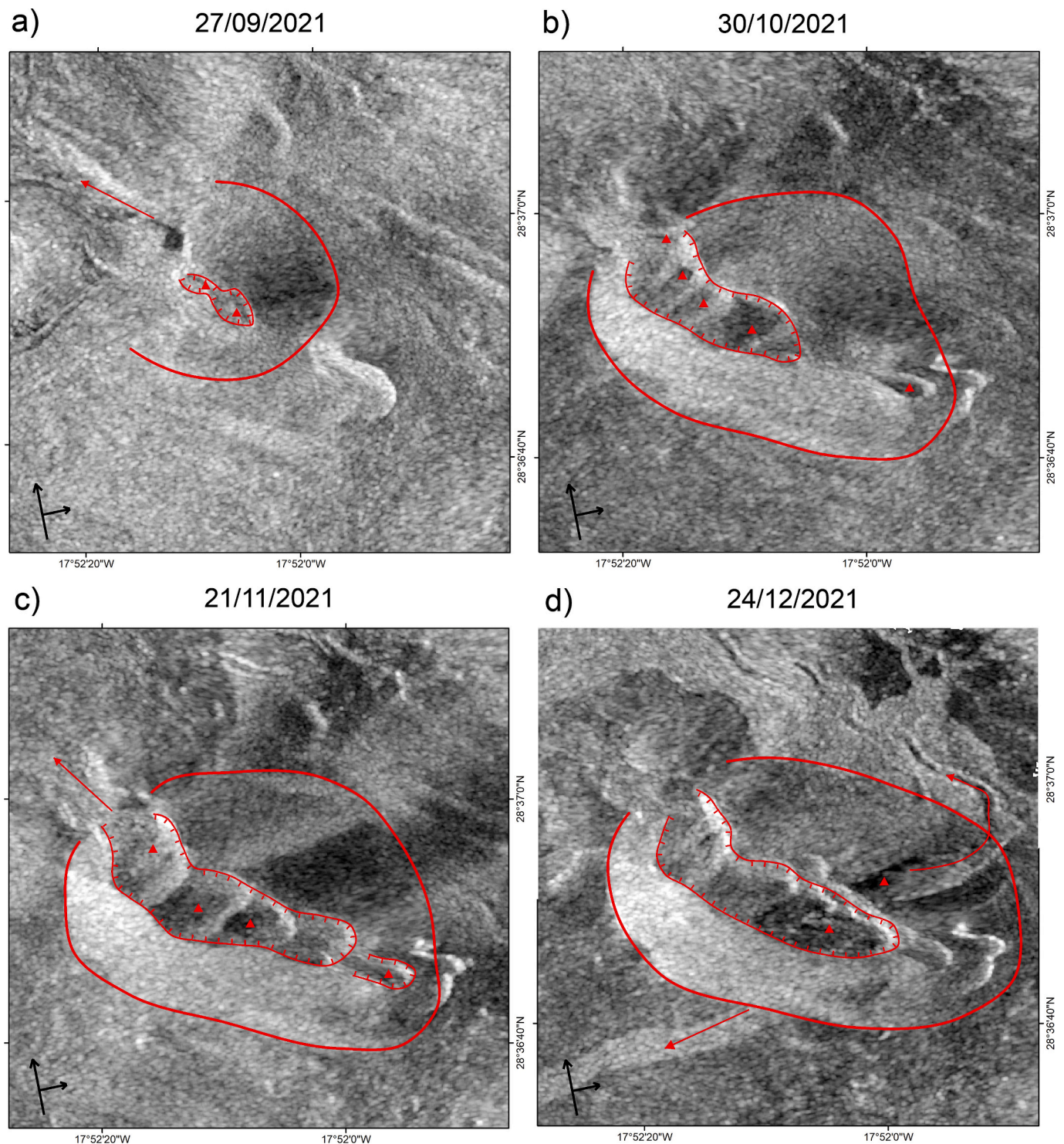
Fig. 8. Cone morphology evolution using PAZ Stripmap (3 m Resolution) in ascending geometry. Red features provide geomorphological interpretation of the cone area (line), vents (triangles), crater cliffs (perpendicular line) and lava flows (arrows). Black arrows indicate the flying and observation directions of the satellite. a) 27/09/2021, b) 30/10/2021, c) 21/11/2021, d) 24/12/2021. (For interpretation of the references to color in this figure legend, the reader is referred to the web version of this article.)

eastern side, urban and natural areas present a green result, and greenhouses on the western side show blue colors. These colors depend on the amplitude changes towards higher values in the east and lower values in the west. In the following days, the lava flows reached the coastline and the lava delta from 1949 eruption (Fig. 10c). Lava flow activity migrated from southern branch (dark blue) to northern one, showing the same color code. The new lava delta is noticed in bright

green. The third map (Fig. 10b) shows higher activity in the North and a new color (dark green-blue) appearing in the South representing lava flows with low activity. Last image (Fig. 10d) is characterized by a reactivation of the South area and the appearance of a new color code: red. Red areas inside the lava flows represent areas "stable" enough to show the high coherence usually related to old lava flows.

At the end of October CSK data was available, including Spotlight
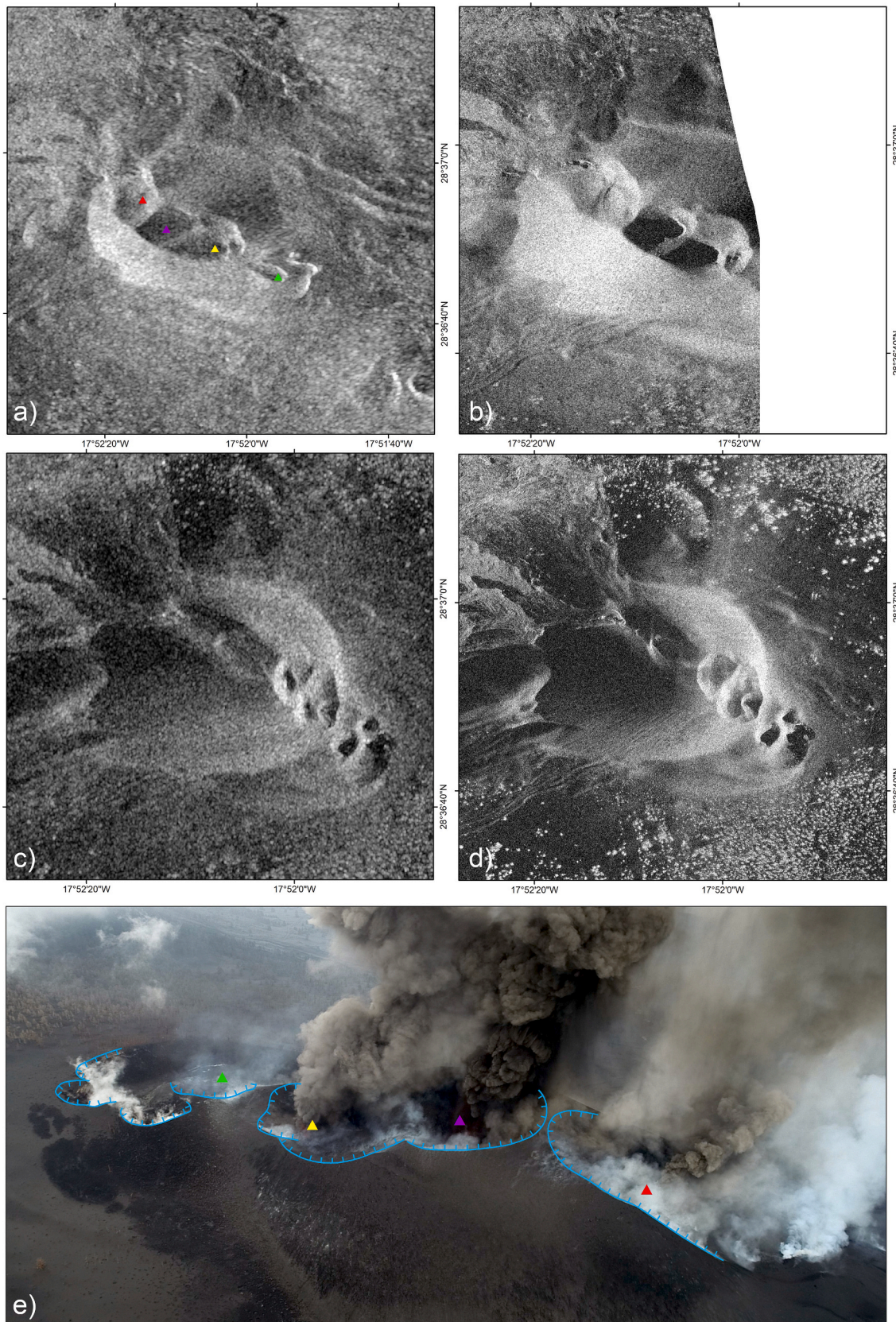
Fig. 9. Differences between Ascending (a, b) and Descending (c, d) Amplitude SAR images from PAZ (a,c, Stripmap 3 m) and CSK (b, d, Spotlight 1 m). e) Cone morphology interpreted using a UAV image and SAR information. Color triangles indicate the location of main vents. All images acquired on 10/11/2021.
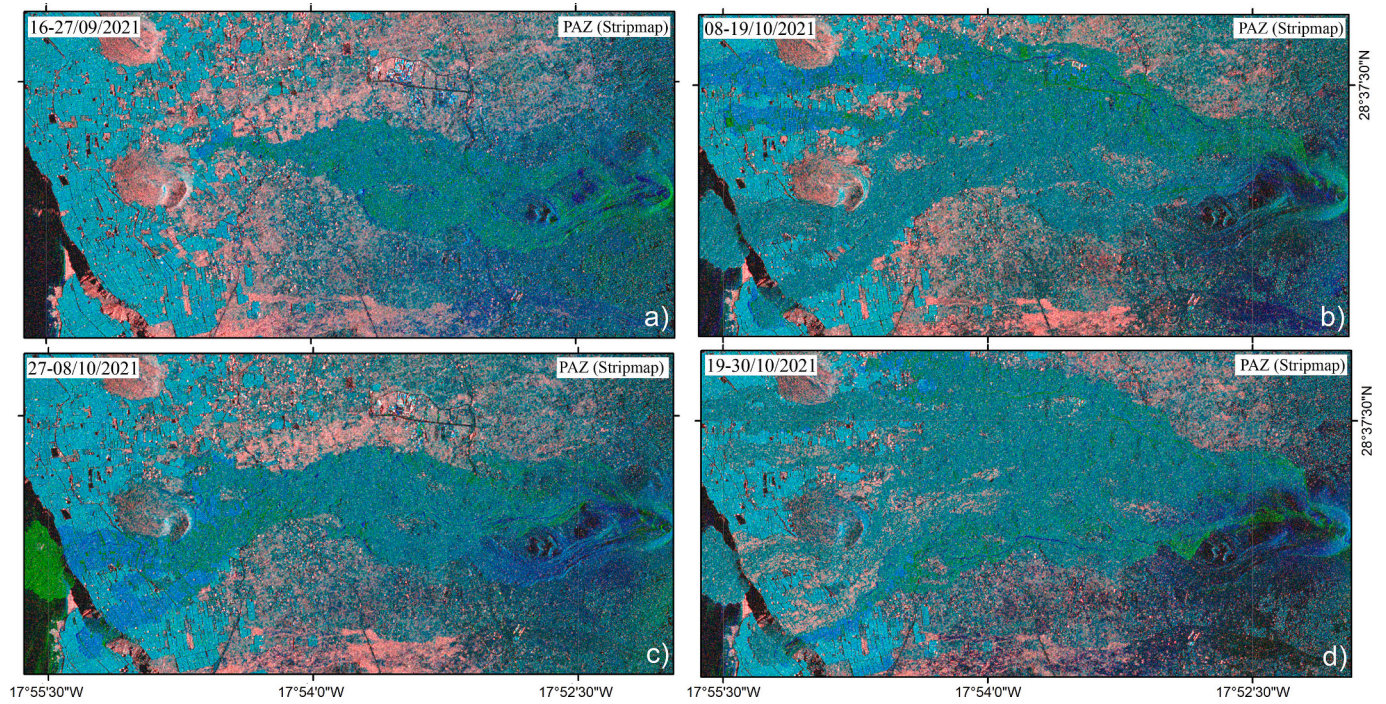
Fig. 10. MTC images obtained using PAZ Stripmap images (3 m, 11 days). a) 16–27/09/2021, b) 08–19/10/2021, c) 27–08/10/2021, d) 19–30/10/2021.
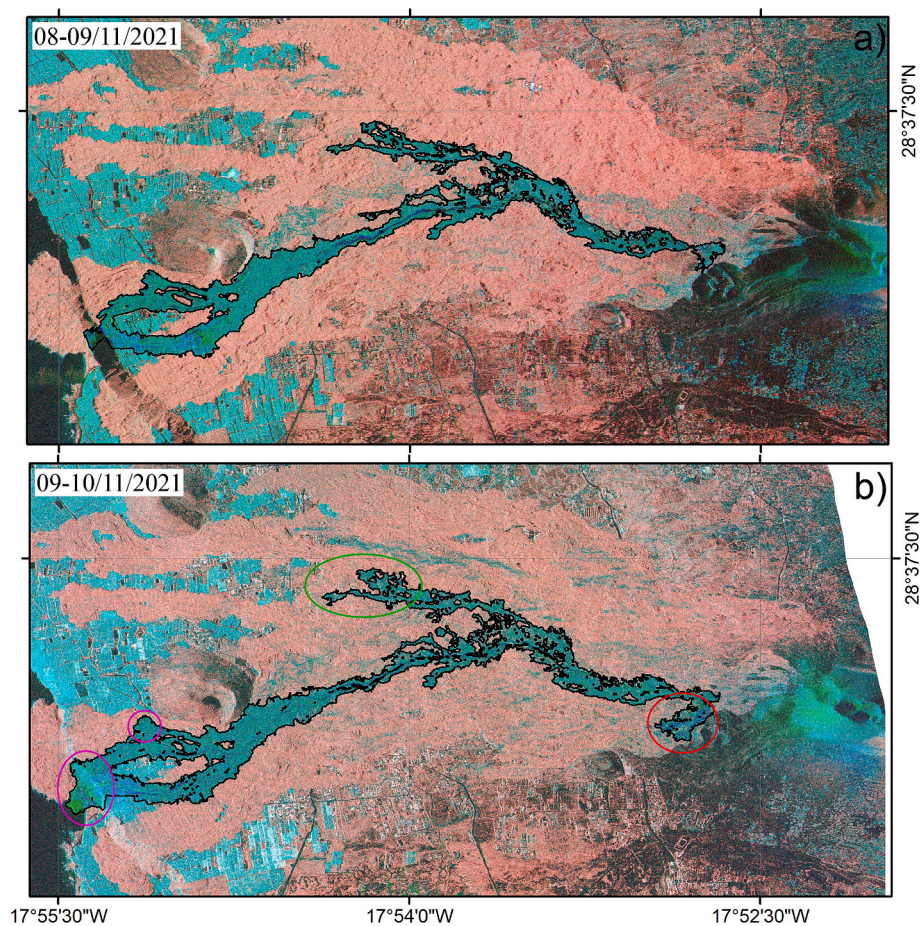
Fig. 11. MTC images obtained using CSK spotlight images (1 m, 1 day). a) 08–09/11/2021, b) 09–10/11/2021.

interferometric data with time gaps of even 1 day. The high temporal resolution reduces the temporal decorrelation, and allowed to detect the active lava channels with great changes inside the slowly changing old lava flows. This product is especially useful for emergency management, supporting the estimation of lava flow evolution only available using thermal data.

The original extension of lava flows is clearly defined in the MTC maps between days 8–9 and 9–10 of October (Fig. 11) by the red area. Dark green-blue areas represent the active channels, with dark blue color over the most active areas and bright blue and green over the areas that were not previously affected. It is clearly seen that main lava flow moves from the effusive vent in the cone mountainside to the area near "Montaña Rajada" trough a lava tube, since no surface lava channel is detected. Changes from Fig. 11a and b are significant near the lava tube outflow where a spill was detected (red circle). Near the coastline a slight advance is detected in the N area, while major advances are noticed over the area between the lava deltas with new lava connecting them (pink circle). Northern branch was stopped and slowly deactivating (green circle). In order to provide a fast delineation of the daily lava

activity for emergency management, an ISO cluster unsupervised classification algorithm was implemented (ArcGIS Support, 2022). Manual post-processing and refinement extracts the active polygon (Fig. 11, black polygons).

MTC maps using images with low time span (less than 6 days, auxiliary data Fig. 12) have proved to be useful to detect the lava flows with recent activity and can be validated using thermal data. Fig. 12a and b are the same image in optical and thermal modes where points 1, 2 and 3 provide spatial references. Points 4 and 7 represent lava channels with dark blue colors in the MTC map (Fig. 12c) and extremely hot values in the thermal data. Points 5 and 6 are side lobes with lower temperature signal and a clear spatial correlation with the dark green-blue MTC areas. This comparison confirms the ability of MTC maps not only to detect the active lava channels but also the side and distal lobes, difficult to identify in the optical inspection. Even if optical data from UAV which was essential during the emergency, it had troublesome to assess the activity of lavas, especially in the distal lobes. That kind of data also requires several flights over the area, expensive in time and machine wearing. SAR data provides a complete overview of the
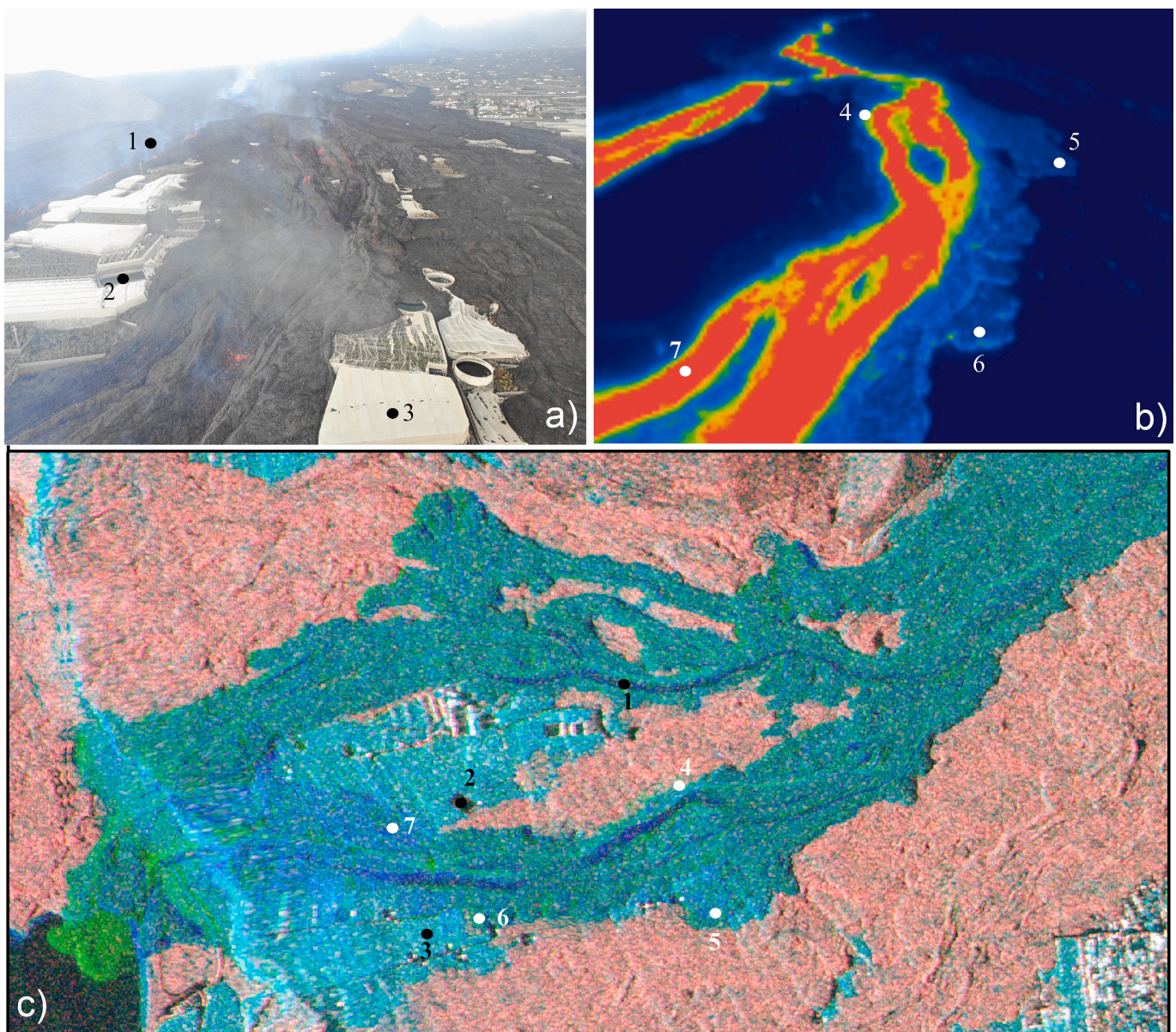
Fig. 12. Comparison between UAV images, optical (a) and thermal (b), and CSK MTC results (c). Black and White numbers represent comparable areas of SAR and UAV data (09–10/11/2021).

area with short processing times.

Accurate demarcation of the lava flow perimeter during the emergency was daily updated by several organizations using direct inspection, UAV, SAR and Optical images. For this reason, the MTC maps generated by the InSARLab team were not used for this task. On the other side, the active lavas location obtained analyzing the MTC maps were a newly developed result that had to be confirmed and validated during the emergency process. Combined with the large data latency of CSK data, low temporal resolution of PAZ (11 days), and Sentinel-1 spatial resolution, the operativity of these results was reduced. Post-analysis of the results revealed them as a powerful tool to reduce the UAV flight time if near daily images are available.

4.3. Regional displacement monitoring

4.3.1. InSAR

Interferograms are the basic product for surface displacement monitoring based on earth observation techniques during a volcanic eruption. Large surface changes associated to an eruption (lava flows, earth fissures, new cone generation) usually reduce the performance of advanced DInSAR techniques because of the sudden coherence change. Interferometric pairs over Canary Islands are usually affected by hard noise effects related to atmospheric artifacts correlated with the topography (Stratified Atmosphere, Hu and Mallorquí, 2019). These effects are common in volcanic islands with steep reliefs (Cao et al., 2021; Hamling, 2021; Liang et al., 2021) and have not been filtered out from the interferograms obtained during the volcanic event. This option was chosen to maintain the closeness with the decision-making staff

providing them the information in the minimum time gap.

The fissure eruption on September 19th was registered by two interferometric Sentinel-1 pairs, one on each acquisition geometries. Ascending interferogram (Fig. 13a), from September 14th to September 20th, shows a clear displacement field towards the satellite of at least 11 fringes and a small lobe north of the vents of 1 fringe away from the satellite. Since one fringe means half the wavelength (5.6 cm in the case to Sentinel-1), the estimated displacement of the SW lobe was about 30 cm, in accordance with the accumulated displacement in LP03 GNSS permanent station (Fig. 13; IGN, 2022b). Descending results (Fig. 13b), from September 16th to September 22nd, provide a more complex interferogram with two lobes towards the satellite (N and S) and two away (E and W). Detected displacement would be compatible with an intrusive dyke laying towards NE that generated a NW-SE fissure with various vents (De Luca et al., 2022). This model is also coherent with the depth and location evolution of the earthquakes (Fig. Supl. 1; IGN, 2022a).

After the beginning of the eruption, displacements were monitored using regular Sentinel-1 acquisitions each 6 days in both geometries including 20 interferograms on each (Fig. Supl. 2 and 3). Interferograms were analyzed joint with information from in-situ monitoring data available (GNSS stations, extensometers, tiltmeters), visual information from field staff and other data from satellites (Pleiades, VIIRS). All the anomalies detected after the co-eruptive interferograms showed no significant signals to be considered as confirmed displacement. The results are confirmed by the stable trend measured by IGN GNSS stations. One of those permanent stations (LP03) registered 6 episodes of sudden vertical displacement (Fig. 16). They were not observed in the Sentinel-1
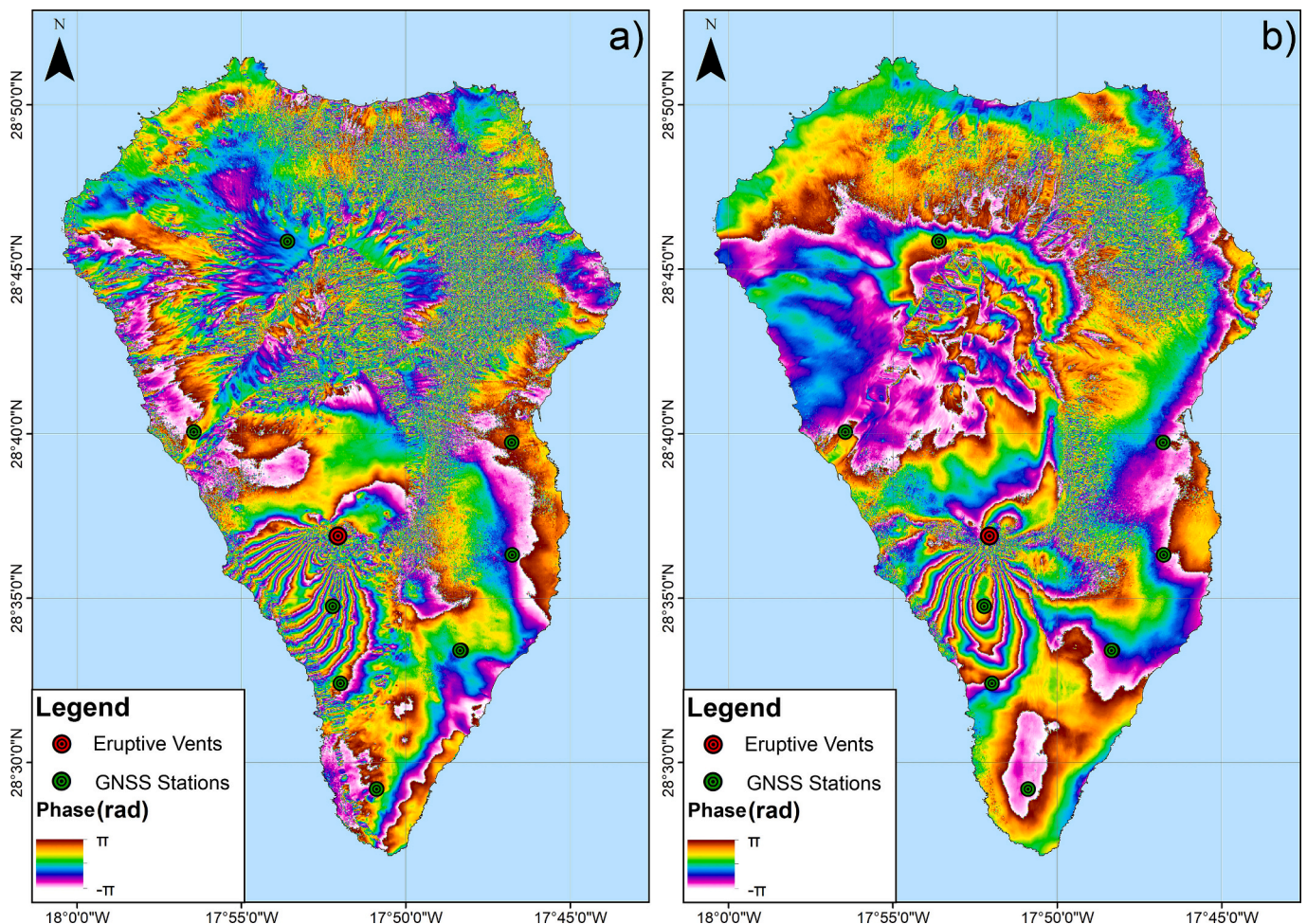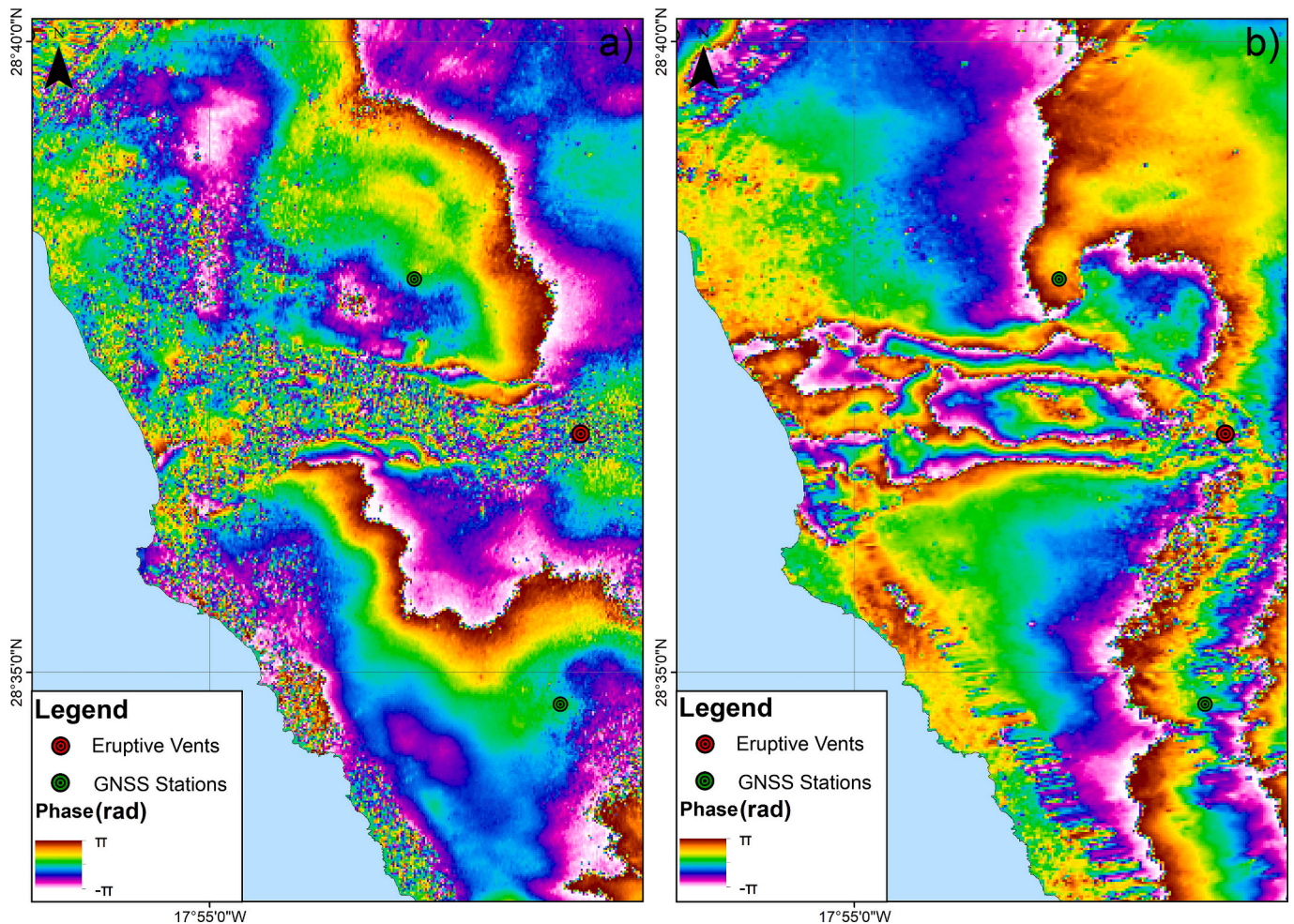

Fig. 13. Co-eruptive interferograms in ascending (a) and descending (b).

Fig. 14. Lava compaction during the eruption (a, 21–27th October) and after its end (b, 31st December – 12th January). Sentinel-1 ascending data.

interferograms probably because were caused by very local displacements.

Distal inactive areas of the lava flows began to cool without new lava intakes, showing the first coherent data in the edges on October 21st (Fig. 14a) and all over the lava flows after the eruption end on December 13th (Fig. 14b). Interferograms after that date reveals a continuous subsiding trend in the lava flows according to their natural contraction while progressively cooling.

Interferometric results from Sentinel-1 were obtained each time a new image was ready to use. Once available at the Sentinel-1 repositories, around 1 h after acquisition, the shortest interferometric pair was calculated and analyzed. Results and first conclusions were reported to the in-situ field team. Displacement anomalies were compared with GNSS data. Local anomalies detected in-situ were communicated to the remote sensing team and analyzed in the interferometric results using both Sentinel-1 and high-resolution data available.

4.3.2. MT-DInSAR

The descending geometry was chosen to avoid the severe foreshortening that would result from the steep slopes of the western flank of Cumbre Vieja (González et al., 2010). The coherence threshold for Measurement Points (MP) selection was 0.80 in the case of P-SBAS and for initial PS selection in SNAPPING was 0.40. The total number of pixels detected for each processing was 49,564 DS and 31,405 PS, resulting in a pixel density of 70 MP/km^2 and 44.35 MP/km^2 respectively. Fig. 15 show the mean LOS velocity maps of the island of La Palma obtained for each processing. The mean LOS velocities range from 1.85 to −1.40 cm/year for the P-SBAS processing and from 2.64 to −1.96 cm/year for

SNAPPING. Negative and positive values indicate movement away and towards the satellite, respectively. Maximum deformation towards the satellite is located in the western flank of Cumbre Vieja, at the south of the eruptive vents.

Both datasets show good agreements in terms of deformation spatial distribution, having higher mean velocity values the SNAPPING processing because the studied period is shorter. The complete time series of both datasets in a 200 m buffer around the LP03 permanent GNSS station from the IGN regional network (located in the area of maximum displacements) are shown in Fig. 16. The SNAPPING displacement time series were smoothed using a moving average window of three acquisitions, but only before and after the eruptive event to maintain the discontinuity due to the volcano activity. Displacements also show good agreement (Fig. 16). Pre-event period has a linear trend with oscillations in a range of less than 3 cm. Between the acquisition dates 10/09/2021 to 22/09/2021, both algorithms detect an uplift discontinuity of 14.5 cm and 16 cm in LOS. We have also compared the retrieved MT-DInSAR displacements with the measurements of the LP03 permanent GNSS station, which have been projected in the LOS of the satellite. Good agreement MT-DInSAR-GNSS and also with publication of De Luca et al. (2022), which uses the same processing chain and slightly different time period (16/01/2017 to 04/10/2021).

5. Discussion

SAR data from 4 different satellites has been used to generate three SAR-derived products to monitor the evolution of the morphology of the volcanic building, the extension of lava flows and ground deformation
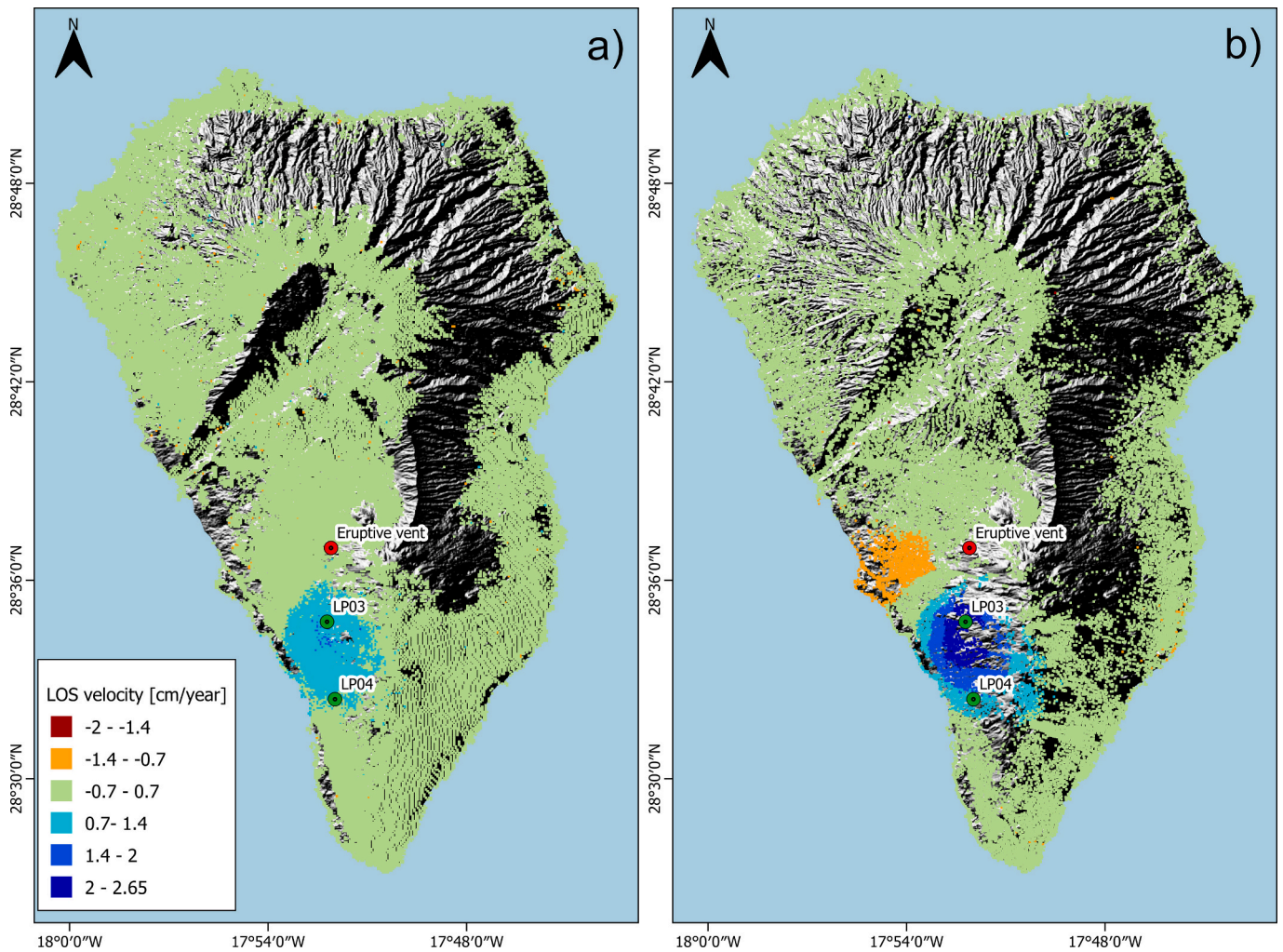
Fig. 15. Mean LOS velocity maps obtained using the P-SBAS (a) and SNAPPING (b) processing chains in the GEP.
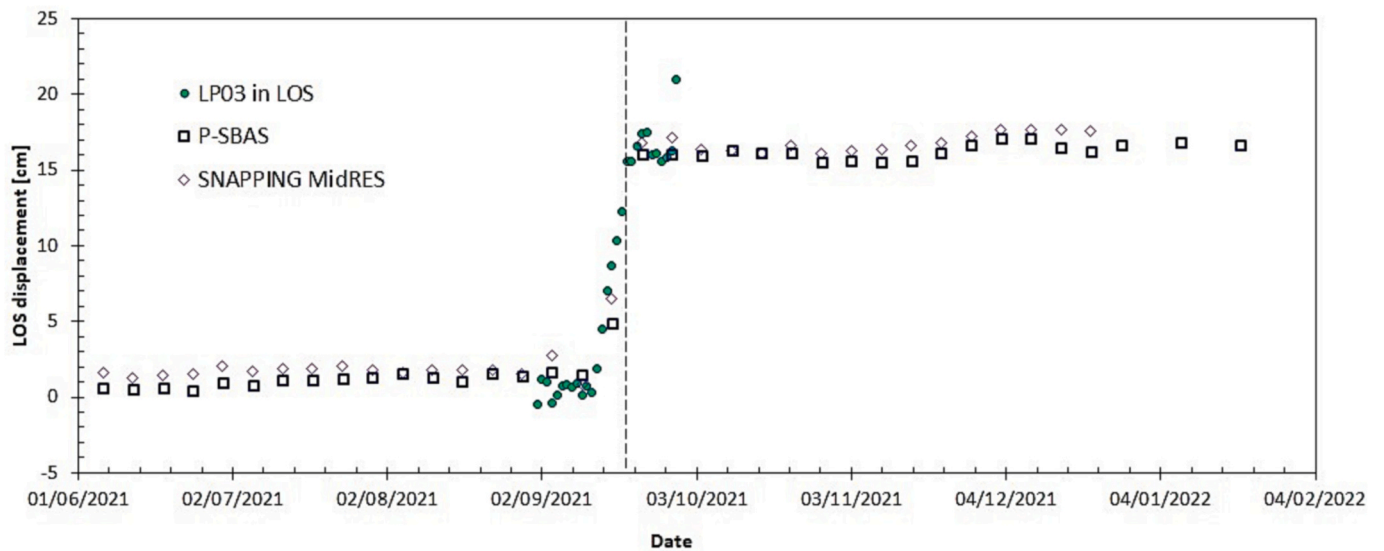
Fig. 16. Comparison of LOS displacement time series with the GNSS displacements projected in LOS of the LP03 permanent station. GNSS data from IGN (2022b).

evolution in time. The availability of data from various satellites with different characteristics (spatial and temporal resolution, wavelength band) allows for their comparison identifying which is the optimal

satellite and/or SAR dataset to generate each result.

Accessibility refers to the easy, quick and continuous access to the SAR images necessary for the operative use of the data during the

emergency management. Difficulties, delays and uncertainties reduce the operativity of the products.

In this analysis we evaluate the technical performance and the accessibility to data. The technical performance measures the quality of each SAR derived result to map and monitor volcanic features, whereas the accessibility to data evaluates the velocity at which SAR images are available during the emergency.

To evaluate the technical performance result we consider two variables:

(1) Detection capacity: this binary variable evaluates if the satellite SAR data is useful (1, capable) or not (0, not capable) to generate the targeted SAR-result. Note that during La Palma crisis Capella satellite did not allow to generate InSAR – phase products because of the satellite configuration.

(2) Quality of the result: expert criterion is used to assess this variable in Low, Medium or High quality (1/2/3). Note that this assessment is based on the usefulness of the SAR – derived result which depends not only on the spatial resolution of the images.

In our case study, the best quality (level 3) regarding the morphology of the volcanic edifice is achieved using the Capella and CSK-Spotlight data (Table 3). Cone morphology analysis based on SAR amplitude data takes advantage of the spatial resolution. Ultra-high resolution of Capella satellites (0.5 m) data allows to interpret most of the cone and lava flow features (vents, cliffs, channel levees, cracks) even better than UAV photo-interpretation (Fig. 17a, e and f). Capella data increase the contrast revealing occult features and is not affected by ash plume. Other source of high resolution data are CSK and PAZ constellations. They operate in two modes (spotlight and stripmap) both useful for the cone morphological characterization but preferring spotlight due to higher resolution (Fig. 17). Stripmap data (Fig. 17b and c) still reveals most of the features detected by UAV avoiding that technique limitations. Sentinel-1 amplitude images (Fig. 17d) have lower resolution, only allowing to see the main shapes.

The best quality lava flow detection products are produced using CSK-Spotlight products (Table 3). The detection of lava flow perimeters and active areas uses interferometric coherence, to generate false color MTC maps. Rough external perimeter is easily detected by all the satellites due to the significant changes between the areas affected by lavas from those that are not. Higher resolution data implies clearer and sharpen features visualizations, but a good product is achievable using Sentinel-1 data (Fig. 18a and d). Capella data provides high resolution information about the lava flow activity based on amplitude data but lack of interferometric capabilities during this event prevent to apply the MTC technique. Active lava flow delineation capability is more dependent of temporal resolution than spatial resolution. PAZ data (11 days revisiting period) were useful during the first stages of the event, but they provide less information for the acquisitions recorded after that the area was covered by lava flows at the end of October (Fig. 18b). Old cooling lavas can be detected in the PAZ results as the red areas beginning to appear in the distal areas and the most active lavas are seen in blue and green colors (Fig. 18b). Relevance of this data declines as it

shows the change of the last 11 days, usually with a low significance in the emergency management. Sentinel-1 results provide a rough estimation, which is limited due to spatial and temporal resolution (Fig. 18a). 6-days MTC maps allow for differentiating active (green-blue) and inactive (red) areas. Best results were achieved using CSK data (Fig. 18c): 1-day interferometrical results accurately show that the activity of most of the lava flows is low (red), whereas the active channels show a different behavior. This product is useful for daily monitoring the lava flows and activity planning but is not always available due to CSK constellation characteristics.

The best quality volcanic ground deformation products are generated by Sentinel-1 data (Table 3). Ground displacements can reveal the first signals of an eruptive process, also providing valuable information after the eruption to detect anomalies. In the case of fissure eruption like in La Palma case study, the opening of new vents could be anticipated by using interferometric results. Both C-band (Sentinel-1) and X-band (PAZ and CSK) were used to generate interferograms useful to detect regional displacements (Fig. 19) during the eruption process.

Sentinel-1 data (Fig. 19a) are capable to provide interferograms less affected by topographic and atmospheric effects (accumulation of fringes in the island ranges in Fig. 19b) than X-band data (Fig. 19b), resulting in less decorrelated areas (blur areas in Fig. 19). Even if theoretically X-band data could be useful to detect local anomalies, the topographic and atmospheric related errors prevent an adequate interpretation of the displacement patterns. Contrarily lava flow cooling compaction, is as a phenomenon limited to a well-defined area that takes advantage of the high resolution and sensitivity of X-band data avoiding the influence of the errors impacting the regional analysis.

To assign the level of technical capability, we use Eq. (1), which can result in final values 0, 1, 2, 3 (0 no technical capability, 1 low, 2 medium, 3 high)

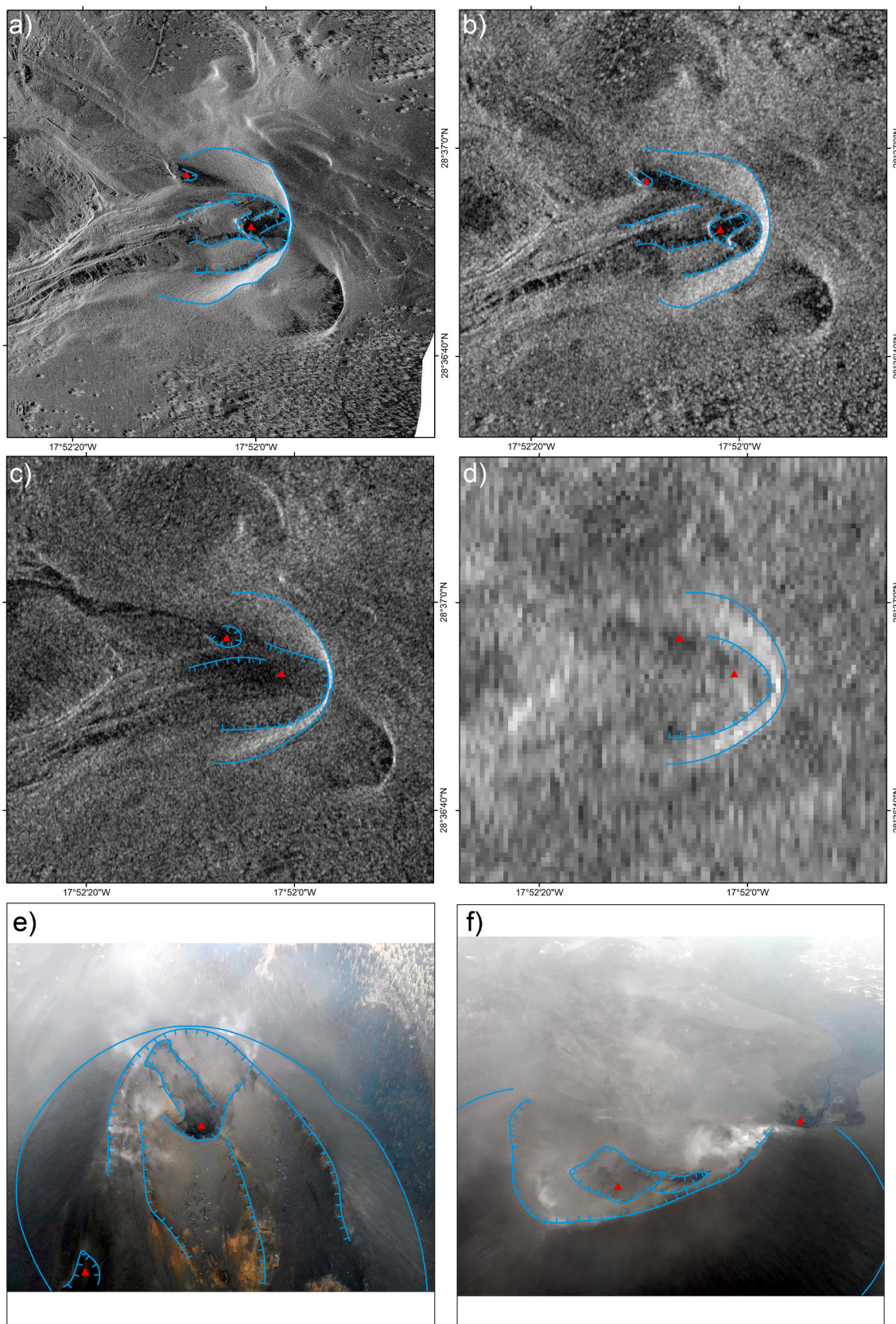$$Technical\ Capability = Detection*Quality \tag{1}$$

Table 3 shows the results for each dataset.

The other aspect we have evaluated is data accessibility, which refers to the easy, quick and continuous access to the SAR images that are necessary to support the emergency management. During an emergency scenario any difficulty, delay or uncertainty for accessing the data for every study area will reduce the usefulness of the retrieved results. Accessibility depends not only in the satellite characteristics but in the way of access that user have to the data. The potential of the methodology is that describes different possibilities that can be re-evaluated by any team working in emergencies depending on their possibilities. The results can be also easily recalculated if data access circumstances change during the emergency allowing to optimize the resources. Data accessibility is considered using 3 factors, and evaluated for La Palma case study in Table 4:

- Data access: to evaluate the availability of satellite data: Open Access (3) refers to free access services, such as Copernicus Open Access Hub; Continuous access (2) refers to the private access to platforms or FTP services during the emergency; Discontinuous access (1) refers to data offered by data providers without temporal continuity.

Table 3
Technical capability assigned to each SAR data to generate each monitoring product.

TECHNICAL CAPABILITY								
	Morphology of the volcanic edifice			Lava flow detection			Volcanic ground deformation		
SAR DATA	Detection (1/0)	Quality (1/2/3)	Technical cap.	Detection (1/0)	Quality (1/2/3)	Technical cap.	Detection (1/0)	Quality (1/2/3)	Technical cap.
Capella	1	3	3	1	1	1	0	0	0
CSK-Spot	1	3	3	1	3	3	1	1	1
CSK-Strip	1	2	2	1	2	2	1	1	1
Paz	1	2	2	1	2	2	1	1	1
S-1	1	1	1	1	1	1	1	3	3

Fig. 17. Comparison of SAR Amplitude images from different satellites, a) Capella (27/09/2021) b) PAZ (27/09/2021) c) CSK (27/09/2021), d) Sentinel-1 (28/09/2021), e) and f) UAV optical image (27/09/2021). Blue lines show morphological features identified: Straight line for the cone perimeter, crossed line for cliffs and red triangles for vents. Capella imagery is copyright of the Capella Space company, all rights reserved. (For interpretation of the references to color in this figure legend, the reader is referred to the web version of this article.)
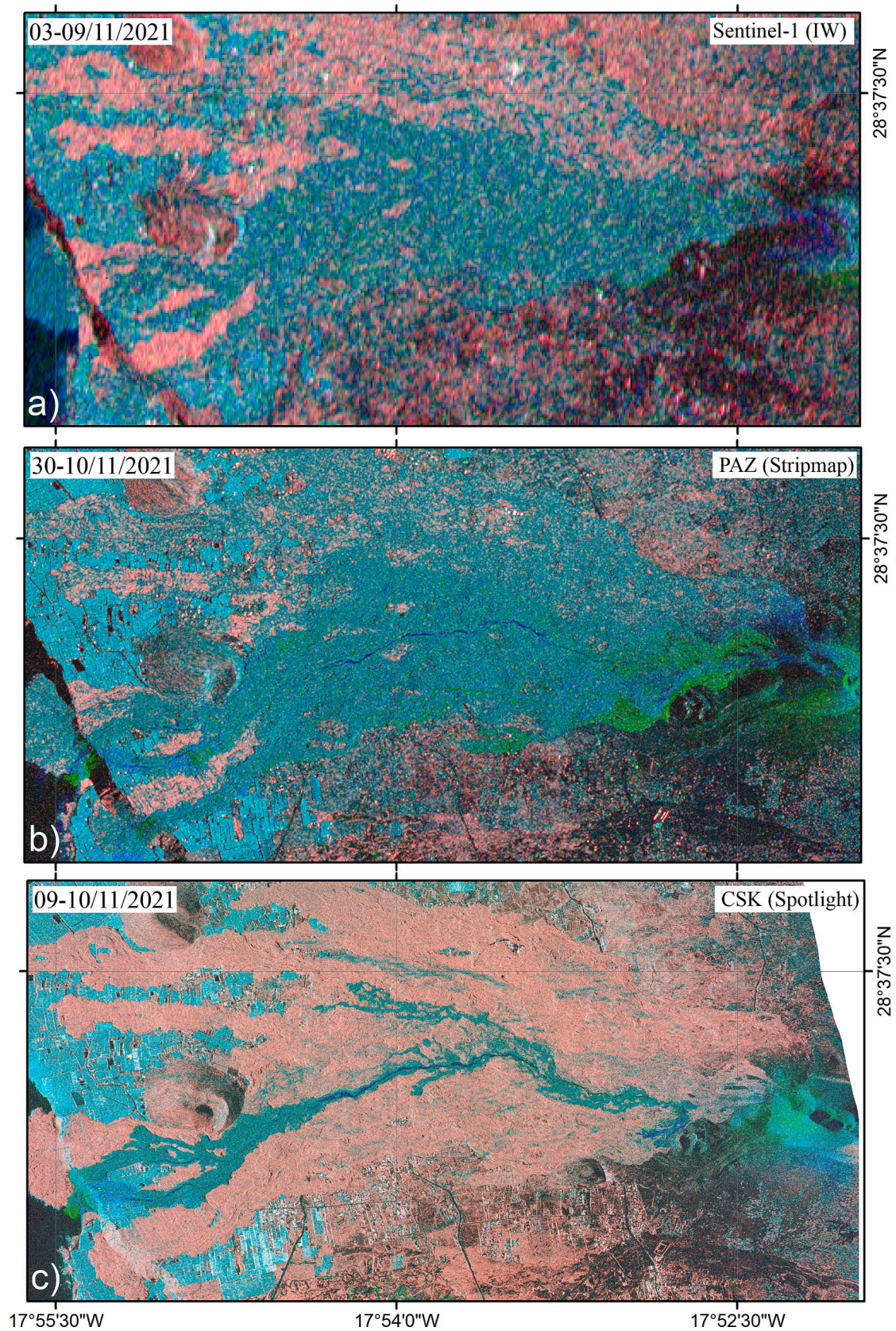
Fig. 18. Comparison of MTC images from different satellites and available time gaps, a) Sentinel-1, 6 days b) PAZ, 11 days c) CSK, 1 day.
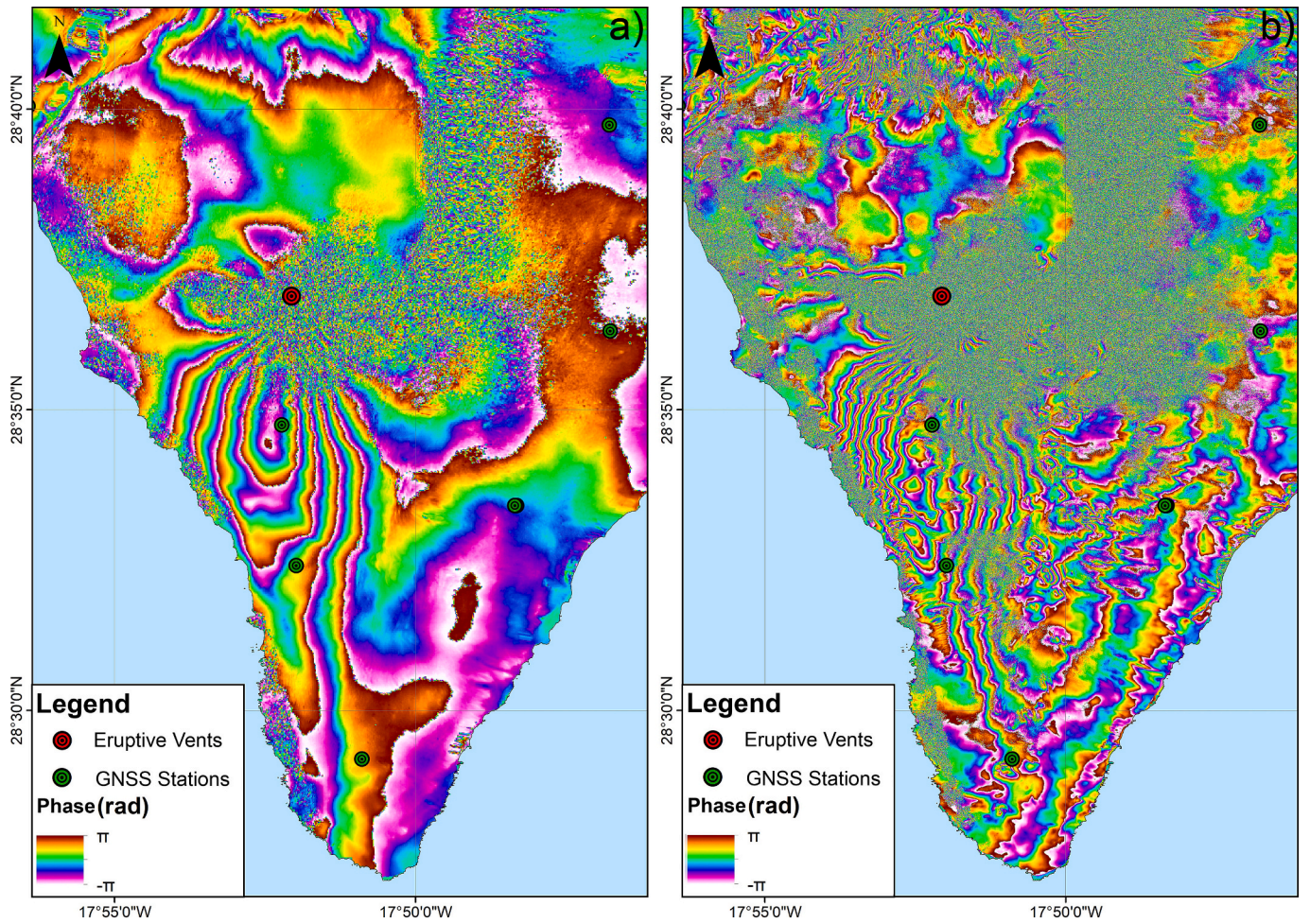
Fig. 19. Descending interferograms from Sentinel-1 (a) and PAZ (b). S1 ML6x2 G1. PAZ ML3x3 G1.

Table 4
Accessibility values assigned to each SAR data.

ACCESIBILITY					
SAR DATA	Capella	CSK-Spot	CSK-Strip	Paz	S-1
Access	1	1	1	2	3
Latency	1	1	1	1	2
Acquisition Cycle	1	2	2	2	2
Accessibility	0.375	0.5	0.5	0.625	0.875

- Data Latency: to express the time gap between data acquisition and user receipt, being either hours (2) or days (1).
- Acquisition Cycle: to assess data repeatability and consistency of the acquisition. Being continuous and on-demand (3), continuous (2) or discontinuous (1).

To assign the accessibility value, we use Eq. (2).

$$Accessibility = \frac{Access + Latency + Acq.Cycle}{Max\ Value} \qquad (2)$$

where *Max Value* is equal to 8.

Table 4 shows the results for each dataset.

Finally, to evaluate the most appropriate dataset (operativity), we combine both factors (Eq. (3)):

$$Operatibity = Accessibility * Technical\ Capacities \qquad (3)$$

Considering both, accessibility and technical capacity, the optimal

Table 5
Analysis of the best SAR data available (highest operativity) to generate each product.

OPERATIVITY					
SAR DATA	Capella	CSK-Spot	CSK-Strip	Paz	S-1
Morphology of the volcanic edifice	1.125	**1.5**	1	1.25	0.875
Lava flow detection	0.375	**1.5**	1	1.25	0.875
Volcanic ground deformation	0	0.5	0.5	0.625	**2.625**

SAR dataset to generate each product are shown in Table 5. Operativity values are dimensionless and must be considered only for ranking purposes. The optimal (most operative) SAR data to monitor changes in the volcano morphology and the evolution of lava flow are CSK- spotlight data. Sentinel-1 data are the best option to monitor volcanic ground deformation. The strength of the products described here lies in the possibility to generate them for other volcanic emergencies, even when the most optimal dataset is not available. Here we have shown how they can be produced using different platforms, achieving different operativity levels.

6. Conclusions

After three months of uninterrupted volcanic eruption many options to extract information from SAR data were considered and developed. Most of them were inadequate to produce updated information with the

timeliness that emergency management requires but provided valuable data to take decisions. During the event only regional displacements monitoring was operationally used in the management cycle, while most of the other data were used to alert field researchers and technicians of possible anomalies or check their early-warnings on field.

Cone morphology monitoring is highly dependent of spatial resolution, taking advantage of X-band satellites, but the delays between acquisition and processing reduced their operativity during the emergency. Despite that, the data were useful to locate new vents and cone features over areas covered by the volcanic plume. Lava flow analysis through MTC maps resulted in a new and efficient tool to monitor new lava flows over older ones. Daily CSK data are the best option for this purpose with the combination of high spatial and temporal resolution. This product can be especially useful during emergencies over populated areas to detect new lava spills. Finally, ground displacements have been observed using Sentinel-1 data at regional scale, with high quality due to their good resolution and easy accessibility. This knowledge is very useful for the teams working with SAR data during the emergency, since it would help to make more efficient decisions when interacting with data providers.

In comparison with other data sources like UAV-based sensors and in-situ measurements, SAR images provide results over larger areas with lower requirements of staff, time and equipment. However, UAV and in-situ measurements are essential to validate the information inferred from SAR data and perform in-detail local analysis.

Supplementary data to this article can be found online at https://doi.org/10.1016/j.rse.2023.113668.

Authors contribution

P.E., G.B and M.B.P. conceived, coordinated and wrote the manuscript in collaboration with all the coauthors. P.E. and G.B. processed InSAR data. E.G.A. and R.G. provided and analyzed GNSS and SAR data, respectively. P.E., G.B., M.B.P. and O.M. analyzed InSAR results. I.G., J.C.L.D., N.S., I.M., R.P. R.M.M., R.P.L, C.G.A., J.L.V., J.A.F.M. and G.E. analyze the products and discussed their usefulness. All authors were involved in developing the presented ideas and reviewed the manuscript.

Declaration of Competing Interest

The authors declare that they have no known competing financial interests or personal relationships that could have appeared to influence the work reported in this paper.

Data availability

The authors do not have permission to share data.

References

Afonso, A., 1974. Geological Sketch and Historic Volcanoes in La Palma, Canary Islands. Estudios Geológicos, Teneguia Volume, pp. 7–13.

Albino, F., Biggs, J., Escobar-Wolf, R., Naismith, A., Watson, M., Phillips, J.C., Marroquin, G.C., 2020. Using TanDEM-X to measure pyroclastic flow source location, thickness and volume: application to the 3rd June 2018 eruption of Fuego volcano, Guatemala. J. Volcanol. Geotherm. Res. 406, 107063.

Alonso-González, A., Gimeno, N., Hajnsek, I., Cifuentes, P., González, M.J., Grigorov, C., Roth, A., Marschalk, A., Casal, N., Cuerda, J.M., García, M., 2021. Joint PAZ & TanDEM-X mission interferometric experiments: interoperability and products. IEEE J. Sel. Top. Appl. Earth Obs. Remote Sens. 14, 6069–6082. https://doi.org/10.1109/JSTARS.2021.3084401.

Ancoechea, E., Hernán, F., Cendrero, A., Cantagrel, A., Fuster, J.M., Ibarrola, E., Coello, J., 1994. Constructive and destructive episodes in the building of a young oceanic islands. La Palma Canary Islands and genesis of the Caldera de Taburiente. J. Volcanol. Geotherm. Res. 60, 243–622.

ArcGIS Support, 2022. Description of the ArcGIS tool "Iso Cluster Unsupervised Classification". Last Access: 09/02/2022. Available at: https://desktop.arcgis.com/en/arcmap/latest/tools/spatial-analyst-toolbox/iso-cluster-unsupervised-classification.htm.

Arnold, D.W., Biggs, J., Anderson, K., Vallejo Vargas, S., Wadge, G., Ebmeier, S.K., Mothes, P., 2017. Decaying lava extrusion rate at El Reventador volcano, Ecuador, measured using high-resolution satellite radar. J. Geophys. Res. Solid Earth 122 (12), 9966–9988. https://doi.org/10.1002/2017JB014580.

Arnold, D., Biggs, J., Wadge, G., Mothes, P., 2018. Using satellite radar amplitude imaging for monitoring syn-eruptive changes in surface morphology at an ice-capped stratovolcano. Remote Sens. Environ. 209, 480–488.

Auker, M.R., Sparks, R.S.J., Siebert, L., Crosweller, H.S., Ewert, J., 2013. A statistical analysis of the global historical volcanic fatalities record. J. Appl. Volcanol. 2, 1–24.

Baker, S., Amelung, F., 2012. Top-down inflation and deflation at the summit of Kīlauea volcano, Hawai 'i observed with InSAR. J. Geophys. Res. Solid Earth 117 (B12).

Bellido Mulas, F., Gómez Sainz de Aja, J.A., Barrera, J.L., 2023. Mapa Geológico Digital continuo E. 1: 25.000, Zona Canarias - La Palma. (Zona-2915). In: GEODE. Mapa Geológico Digital continuo de España. Online. Last Access: 09/02/2022. Available at: http://info.igme.es/cartografiadigital/geologica/geodezona.aspx?Id=Z2915.

Berardino, P., Fornaro, G., Lanari, R., Sansosti, E., 2002. A new algorithm for surface deformation monitoring based on small baseline differential SAR interferograms. IEEE Trans. Geosci. Remote Sens. 40 (11), 2375–2383.

Biggs, J., Wright, T., Lu, Z., Parsons, B., 2007. Multi-interferogram method for measuring interseismic deformation: Denali fault, Alaska. Geophys. J. Int. 170, 1165–1179. https://doi.org/10.1111/j.1365-246X.2007.03415.

Bignami, C., Corradini, S., Merucci, L., de Michele, M., Raucoules, D., De Astis, G., Stramondo, S., Piedra, J., 2014. Multisensor satellite monitoring of the 2011 Puyehue-Cordon Caulle eruption. IEEE J. Sel. Top. Appl. Earth Obs. Remote Sens. 7 (7), 2786–2796.

Boccardo, P., Gentile, V., Tonolo, F.G., Grandoni, D., Vassileva, M., 2015. Multitemporal SAR coherence analysis: Lava flow monitoring case study. In: Proceedings 2015 IEEE International Geoscience and Remote Sensing Symposium (IGARSS). IEEE, pp. 2699–2702.

Cabildo La Palma, 2022. https://riesgovolcanico-lapalma.hub.arcgis.com/ (Last accessed 04/10/2022).

Camacho, A.G., Fernández, J., González, P.J., Rundle, J.B., Prieto, J.F., Arjona, A., 2009. Structural results for La Palma Island using 3-D gravity inversion. J. Geophys. Res. 114 (B5) https://doi.org/10.1029/2008JB005628.

Cao, Y., Jónsson, S., Li, Z., 2021. Advanced InSAR tropospheric corrections from global atmospheric models that incorporate spatial stochastic properties of the troposphere. J. Geophys. Res. Solid Earth 126. https://doi.org/10.1029/2020JB020952.

Carracedo, J.C., 1994. The Canary Islands: An example of structural control on the growth of large oceanic-island volcanoes. J. Volcanol. Geotherm. 60 (3–4), 225–241. https://doi.org/10.1016/0377-0273(94)90053-1. ISSN 0377-0273.

Carracedo, J.C., Badiola, E.R., Guillou, H., De la Nuez, J., Pérez Torrado, F.J., 2001. Geology and volcanology of La Palma and El Hierro, Western Canaries. Estud. Geol. 57, 175–273. https://doi.org/10.3989/egeol.01575-6.

Castelletti, D., Farquharson, G., Stringham, C., Duersch, M., Eddy, D., 2021. Capella space first operational SAR satellite. In: 2021 IEEE International Geoscience and Remote Sensing Symposium IGARSS, pp. 1483–1486. https://doi.org/10.1109/IGARSS47720.2021.9554100.

Casu, F., Elefante, S., Imperatore, P., Zinno, I., Manunta, M., De Luca, C., Lanari, R., 2014. SBAS-DInSAR parallel processing for deformation time-series computation. IEEE J. Sel. Top. Appl. Earth Obs. Remote Sens. 7 (8), 3285–3296.

Civico, R., Ricci, T., Scarlato, P., et al., 2022. High-resolution digital surface model of the 2021 eruption deposit of cumbre vieja volcano, La Palma, Spain. Sci. Data 9, 435. https://doi.org/10.1038/s41597-022-01551-8.

Consorcio de Compensación de Seguros, 2022. https://www.consorseguros.es/web/noticias/-/asset_publisher/ya2OdYGgbjgX/content/decimoctava-nota-informativa-so

bre-la-actividad-del-ccs-con-ocasion-de-la-erupcion-volcanica-en-la-isla-la-palma?inheritRedirect=false&redirect=https%3A%2F%2Fwww.consorseguros.es%2Fweb%2Fnoticias%3Fp_id%3D101_INSTANCE_ya2OdYGgbjgX%26p_p_lifecycle%3D0%26p_p_state%3Dnormal%26p_p_mode%3Dview%26p_p_col_id%3Dcolumn-1%26p_p_col_count%3D1 (Last accessed 23/06/2022).

Copernicus EMS, 2022. https://emergency.copernicus.eu/mapping/list-of-components/EMSR546 (Last accessed 04/10/2022).

Covello, F., Battazza, F., Coletta, A., Lopinto, E., Fiorentino, C., Pietranera, L., Valentini, G., Zoffoli, S., 2010. COSMO-SkyMED an existing opportunity for observing the Earth. J. Geodyn. 49 (3–4), 171–180. https://doi.org/10.1016/j.jog.2010.01.001.

Day, S., Carracedo, J.C., Guillou, H., Gravestock, P., 1999. Recent structural evolution of the cumbre Vieja Volcano, La Palma, Canary Islands: volcanic rift zone reconfiguration as a precursor to volcanic flank instability? J. Volcanol. Geotherm. Res. 94 (1–4), 135–167.

De Beni, E., Cantarero, M., Messina, A., 2019. UAVs for volcano monitoring: A new approach applied on an active lava flow on Mt. Etna (Italy), during the 27 February–02 march 2017 eruption. J. Volcanol. Geotherm. Res. 369, 250–262.

De Luca, C., Cuccu, R., Elefante, S., Zinno, I., Manunta, M., Casola, V., Rivolta, G., Lanari, R., Casu, F., 2015. An on-demand web tool for the unsupervised retrieval of earth's surface deformation from SAR data: The P-SBAS service within the ESA G-POD environment. Remote Sens. 7 (11), 15630–15650.

De Luca, C., Valerio, E., Giudicepietro, F., Macedonio, G., Casu, F., Lanari, R., 2022. Pre- and Co-Eruptive Analysis of the September 2021 Eruption at Cumbre Vieja Volcano (La Palma, Canary Islands) Through DInSAR Measurements and Analytical Modeling. Geophys. Res. Lett. 49 (7), e2021GL097293.

Di Traglia, F., Calvari, S., D'Auria, L., Nolesini, T., Bonaccorso, A., Fornaciai, A., Esposito, A., Cristaldi, A., Favalli, M., Casagli, N., 2018. The 2014 effusive eruption at Stromboli: New insights from in situ and remote-sensing measurements. Remote Sens. 10 (12), 2035.

Dietterich, H.R., Poland, M.P., Schmidt, D.A., Cashman, K.V., Sherrod, D.R., Espinosa, A. T., 2012. Tracking lava flow emplacement on the east rift zone of Kīlauea, Hawai 'i, with synthetic aperture radar coherence. Geochem. Geophys. Geosyst. 13 (5).

Dualeh, E.W., Ebmeier, S.K., Wright, T.J., Albino, F., Naismith, A., Biggs, J., Ordoñez, P. A., Boogher, R.M., Roca, A., 2021. Analyzing explosive volcanic deposits from satellite-based radar backscatter, Volcán de Fuego, 2018. J. Geophys. Res. Solid Earth 126 (9), e2021JB022250.

Ebmeier, S.K., Biggs, J., Muller, C., Avard, G., 2014. Thin-skinned mass-wasting responsible for widespread deformation at Arenal volcano. Front. Earth Sci. 2, 35.

Dumont, S., Sigmundsson, F., Parks, M.M., Drouin, V.J.P., Pedersen, G.B.M., Jónsdóttir, I., Höskuldsson, Á., Hooper, A., Spaans, K., Bagnardi, M., Gudmundsson, M.T., Barsotti, S., Jónsdóttir, K., Högnadóttir, T., Magnússon, E., Hjartardóttir, Á.R., Dürig, T., Rossi, C., Oddsson, B., 2018. Integration of SAR Data Into Monitoring of the 2014–2015 Holuhraun Eruption, Iceland: Contribution of the Icelandic Volcanoes Supersite and the FutureVolc Projects. Front. Earth Sci. 6, 231. https://doi.org/10.3389/feart.2018.00231.

Ebmeier, S., Andrews, B., Araya, M., Arnold, D., Biggs, J., Cooper, C., Cottrell, E., Furtney, M., Hickey, J., Jay, J., 2018. Synthesis of global satellite observations of magmatic and volcanic deformation: implications for volcano monitoring & the lateral extent of magmatic domains. J. Appl. Volcanol. 7 (1), 1–26.

Ferretti, A., Prati, C., Rocca, F., 2001. Permanent scatterers in SAR interferometry. IEEE Trans. Geosci. Remote Sens. 39 (1), 8–20.

Ferretti, A., Monti-Guarnieri, A., Prati, C., Rocca, F., Massonnet, D., 2007. InSAR Principles: Guidelines for SAR Interferometry Processing and Interpretation. ESA Publications. European Space Agency. ISBN: 92-9092-233-8.

Foumelis, M., Blasco, J.M.D., Desnos, Y.L., Engdahl, M., Fernández, D., Veci, L., Lu, J., Wong, C., 2018. Esa snap - stamps integrated processing for Sentinel-1 persistent scatterer interferometry. In: IGARSS 2018–2018 IEEE International Geoscience and Remote Sensing Symposium, pp. 1364–1367. https://doi.org/10.1109/IGARSS.2018.8519545.

Foumelis, M., Blasco, J.M.D., Brito, F., Pacini, F., Pishehvar, P., 2021. Snapping for Sentinel-1 mission on geohazards exploitation platform: an online medium resolution surface motion mapping service. In: 2021 IEEE International Geoscience and Remote Sensing Symposium IGARSS, pp. 3991–3994. https://doi.org/10.1109/IGARSS47720.2021.9553893.

Garvin, J.B., Slayback, D.A., Ferrini, V., Frawley, J., Giguere, C., Asrar, G.R., Andersen, K., 2018. Monitoring and modeling the rapid evolution of earth's newest volcanic island: Hunga Tonga Hunga Ha'apai (Tonga) using high spatial resolution satellite observations. Geophys. Res. Lett. 45 (8), 3445–3452.

Global Volcanism Program, 2013. In: Venzke, E. (Ed.), Volcanoes of the World, v. 4.11.1 (18 Aug 2022). Smithsonian Institution. https://doi.org/10.5479/si.GVP.VOTW4-2013. Downloaded 29 Aug 2022.

Goldstein, R.M., Werner, C.L., 1998. Radar interferogram filtering for geophysical applications. Geophys. Res. Lett. 25, 4035–4038. https://doi.org/10.1029/1998GL900033.

González, P.J., Tiampo, K.F., Camacho, A.G., Fernández, J., 2010. Shallow flank deformation at Cumbre Vieja volcano (Canary Islands): Implications for the stability of steep-sided volcano flanks at oceanic islands. Earth Planet. Sci. Lett. 297 (3), 545–557.

González, A.S., Labriola, M., Soteras, J.C., Palma, J.S., Sep. 2011. PAZ instrument design and performance. In: Proc. 3rd Int. Asia-Pac. Conf. Synthetic Aperture Radar, pp. 1–4.

González, P.J., Bagnardi, M., Hooper, A.J., Larsen, Y., Marinkovic, P., Samsonov, S.V., Wright, T.J., 2015. The 2014–2015 eruption of Fogo volcano: geodetic modeling of Sentinel-1 TOPS interferometry. Geophys. Res. Lett. 42 (21), 9239–9246.

Gudmundsson, M.T., Jónsdóttir, K., Hooper, A., Holohan, E.P., Halldórsson, S.A., Ófeigsson, B.G., Aiuppa, A., 2016. Gradual caldera collapse at Bárdarbunga volcano, Iceland, regulated by lateral magma outflow. Science 353 (6296), aaf8988.

Hamling, I., 2021. InSAR observations over the Taupō volcanic Zone's cone volcanoes: insights and challenges from the New Zealand volcano supersite. N. Z. J. Geol. Geophys. 64 (2–3), 347–357. https://doi.org/10.1080/00288306.2020.1721545.

Hjartardóttir, Á.R., Einarsson, P., Gudmundsson, M.T., Högnadóttir, T., 2016. Fracture movements and graben subsidence during the 2014 Bárðarbunga dike intrusion in Iceland. J. Volcanol. Geotherm. Res. 310, 242–252.

Hooper, A., 2008. A multi-temporal InSAR method incorporating both persistent scatterer and small baseline approaches. Geophys. Res. Lett. 35 (16), L16302.

Hooper, A., Bekaert, D., Spaans, K., Arikan, M., 2012. Recent advances in SAR interferometry time series analysis for measuring crustal deformation. Tectonophysics 514-517, 1–13. https://doi.org/10.1016/j.tecto.2011.10.013.

Hu, Z., Mallorquí, J.J., 2019. An accurate method to correct atmospheric phase delay for InSAR with the ERA5 global atmospheric model. Remote Sens. 2019 (11), 1969. https://doi.org/10.3390/rs11171969.

IGN, 2022a. Instituto Geográfico Nacional. Noticias Volcanológicas. https://www.ign.es/web/resources/volcanologia/html/CA_noticias_2021.html (Last accessed 04/10/2022).

IGN, 2022b. Instituto Geográfico Nacional. GNSS Data. https://www.ign.es/web/ign/portal/vlc-gps (Last accessed 04/10/2022).

Jung, J., Kim, D.-J., Lavalle, M., Yun, S.-H., 2016. Coherent change detection using InSAR temporal decorrelation model: A case study for volcanic ash detection. IEEE Trans. Geosci. Remote Sens. 54 (10), 5765–5775.

Klügel, A., Schmincke, H.U., White, J.D.L., Hoernle, K.A., 1999. Chronology and volcanology of the 1949 multi-vent rift-zone eruption on La Palma (Canary Islands). J. Volcanol. Geotherm. Res. 94, 267–282.

Kubanek, J., Richardson, J.A., Charbonnier, S.J., Connor, L.J., 2015a. Lava flow mapping and volume calculations for the 2012–2013 Tolbachik, Kamchatka, fissure eruption using bistatic TanDEM-X InSAR. Bull. Volcanol. 77 (12), 1–13.

Kubanek, J., Westerhaus, M., Schenk, A., Aisyah, N., Brotopuspito, K.S., Heck, B., 2015b. Volumetric change quantification of the 2010 Merapi eruption using TanDEM-X InSAR. Remote Sens. Environ. 164, 16–25.

Kubanek, J., Westerhaus, M., Heck, B., 2017. TanDEM-X time series analysis reveals lava flow volume and effusion rates of the 2012–2013 Tolbachik, Kamchatka fissure eruption. J. Geophys. Res. Solid Earth 122 (10), 7754–7774.

Liang, H., Li, X., Chen, R.-F., 2021. Mapping surface deformation over Tatun volcano group, northern Taiwan using multitemporal InSAR. IEEE J. Sel. Top. Appl. Earth Obs. Remote Sens. 14, 2087–2095. https://doi.org/10.1109/JSTARS.2021.3050644.

Loughlin, S.C., Sparks, R.S.J., Sparks, S., Brown, S.K., Jenkins, S.F., Vye-Brown, C., 2015. Global Volcanic Hazards and Risk. Cambridge University Press.

Lu, Z., Masterlark, T., Dzurisin, D., 2005. Interferometric synthetic aperture radar study of Okmok volcano, Alaska, 2000–2003: magma supply dynamics and postemplacement lava flow deformation. J. Geophys. Res. Solid Earth 110 (B2).

Lundgren, P., Casu, F., Manzo, M., Pepe, A., Berardino, P., Sansosti, E., Lanari, R., 2004. Gravity and magma induced spreading of Mount Etna volcano revealed by satellite radar interferometry. Geophys. Res. Lett. 31 (4).

Mania, R., Walter, T.R., Belousova, M., Belousov, A., Senyukov, S.L., 2019. Deformations and morphology changes associated with the 2016–2017 eruption sequence at Bezymianny Volcano, Kamchatka. Remote Sens. 11 (11), 1278.

Manunta, M., De Luca, C., Zinno, I., Casu, F., Manzo, M., Bonano, M., Fusco, A., Pepe, A., Onorato, G., Berardino, P., 2019. The parallel SBAS approach for Sentinel-1 interferometric wide swath deformation time-series generation: algorithm description and products quality assessment. IEEE Trans. Geosci. Remote Sens. 57 (9), 6259–6281.

Masson, D.G., Watts, A.B., Gee, M.J.R., Urgeles, R., Mitchell, N.C., Le Bas, T.P., Canals, M., 2002. Slope failures on the flanks of the western Canary Islands. Earth Sci. Rev. 57, 1–35.

McAlpin, D., Meyer, F.J., 2013. Multi-sensor data fusion for remote sensing of post-eruptive deformation and depositional features at redoubt volcano. J. Volcanol. Geotherm. Res. 259, 414–423.

Meyer, F., McAlpin, D., Gong, W., Ajadi, O., Arko, S., Webley, P., Dehn, J., 2015. Integrating SAR and derived products into operational volcano monitoring and decision support systems. ISPRS J. Photogramm. Remote Sens. 100, 106–117.

Montgomery-Brown, E.K., Sinnett, D.K., Poland, M., Segall, P., Orr, T., Zebker, H., Miklius, A., 2010. Geodetic evidence for an echelon dike emplacement and concurrent slow slip during the June 2007 intrusion and eruption at Kīlauea volcano, Hawaii. J. Geophys. Res. Solid Earth 115 (B7).

Nakano, T., Kamiya, I., Tobita, M., Iwahashi, J., Nakajima, H., 2014. Landform monitoring in active volcano by UAV and SfM-MVS technique. The international archives of photogrammetry. Remote Sens. Spatial Inform. Sci. 40 (8), 71.

Ozawa, T., Kozono, T., 2013. Temporal variation of the Shinmoe-dake crater in the 2011 eruption revealed by spaceborne SAR observations. Earth Planets Space 65 (6), 527–537.

Pallister, J.S., Schneider, D.J., Griswold, J.P., Keeler, R.H., Burton, W.C., Noyles, C., Newhall, C.G., Ratdomopurbo, A., 2013. Merapi 2010 eruption—chronology and extrusion rates monitored with satellite radar and used in eruption forecasting. J. Volcanol. Geotherm. Res. 261, 144–152.

Plank, S., Walter, T.R., Martinis, S., Cesca, S., 2019. Growth and collapse of a littoral lava dome during the 2018/19 eruption of Kadovar volcano, Papua New Guinea, analyzed by multi-sensor satellite imagery. J. Volcanol. Geotherm. Res. 388, 106704.

Plank, S., Marchese, F., Genzano, N., Nolde, M., Martinis, S., 2020. The short life of the volcanic island new Late'iki (Tonga) analyzed by multi-sensor remote sensing data. Sci. Rep. 10 (1), 1–15.

Poland, M.P., 2014. Time-averaged discharge rate of subaerial lava at Kīlauea volcano, Hawai'i, measured from TanDEM-X interferometry: implications for magma supply and storage during 2011–2013. J. Geophys. Res. Solid Earth 119 (7), 5464–5481.

Poland, M.P., 2022. Synthetic aperture radar volcanic flow maps (SAR VFMs): a simple method for rapid identification and mapping of volcanic mass flows. Bull. Volcanol. 84 (3), 1–11.

Ragona, M., Hannstein, F., Mazzocchi, M., 2011. The financial impact of the volcanic ash crisis on the European airline industry. Chapter 3. In: Alemanno, A. (Ed.), Governing Disasters: The Challenges of Emergency Risk Regulation. Edward Elgar Publishing.

Ruch, J., Wang, T., Xu, W., Hensch, M., Jónsson, S., 2016. Oblique rift opening revealed by reoccurring magma injection in Central Iceland. Nat. Commun. 7 (1), 1–7.

Saepuloh, A., Koike, K., Omura, M., Iguchi, M., Setiawan, A., 2010. SAR-and gravity change-based characterization of the distribution pattern of pyroclastic flow deposits at Mt. Merapi during the past 10 years. Bull. Volcanol. 72 (2), 221–232.

Saepuloh, A., Wikantika, K., Urai, M., 2015. Observing lava dome roughness on synthetic aperture radar (SAR) data: Case study at Mt. Sinabung and Merapi—Indonesia. In: Proceedings 2015 IEEE 5th Asia-Pacific Conference on Synthetic Aperture Radar (APSAR). IEEE, pp. 645–648.

Schaefer, L.N., Di Traglia, F., Chaussard, E., Lu, Z., Nolesini, T., Casagli, N., 2019. Monitoring volcano slope instability with synthetic aperture radar: A review and new data from Pacaya (Guatemala) and Stromboli (Italy) volcanoes. Earth Sci. Rev. 192, 236–257.

Shevchenko, A.V., Dvigalo, V.N., Zorn, E.U., Vassileva, M.S., Massimetti, F., Walter, T.R., Svirid, I.Y., Chirkov, S.A., Ozerov, A.Y., Tsvetkov, V.A., 2021. Constructive and destructive processes during the 2018–2019 eruption episode at Shiveluch volcano, Kamchatka, studied from satellite and aerial data. Front. Earth Sci. 9, 457.

Shreve, T., Grandin, R., Boichu, M., Garaebiti, E., Moussallam, Y., Ballu, V., Pelletier, B., 2019. From prodigious volcanic degassing to caldera subsidence and quiescence at Ambrym (Vanuatu): the influence of regional tectonics. Sci. Rep. 9 (1), 1–13.

Siebert, L., Cottrell, E., Venzke, E., Andrews, B., 2015. Earth's volcanoes and their eruptions: an overview. In: Sigurdsson, H., Houghton, B., McNutt, S.R., Rymer, H., Stix, J. (Eds.), Encyclopedia of Volcanoes, 2nd ed. Academic Press, San Diego, CA, pp. 239–255. https://doi.org/10.1016/B978-0-12-385938-9.00012-2.

Sigmundsson, F., Hreinsdóttir, S., Hooper, A., Arnadóttir, T., Pedersen, R., Roberts, M.J., Feigl, K.L., 2010. Intrusion triggering of the 2010 Eyjafjallajökull explosive eruption. Nature 468 (7322), 426–430.

Sigmundsson, F., Hooper, A., Hreinsdóttir, S., Vogfjörd, K.S., Ófeigsson, B.G., Heimisson, E.R., Eibl, E.P., 2015. Segmented lateral dyke growth in a rifting event at Bárðarbunga volcanic system, Iceland. Nature 517 (7533), 191–195.

Sigurdsson, H., Houghton, B., McNutt, S.R., Rymer, H., Stix, J. (Eds.), 2015. Encyclopedia of Volcanoes, 2nd Ed. Academic Press, San Diego, CA.

Staudigel, H., Feraud, G., Giannerini, G., 1986. The history of intrusive activity on the Island of La Palma (Canary Islands). J. Volcanol. Geotherm. Res. 27, 299–322.

Terunuma, T., Nishida, K., Amada, T., Mizuyama, T., Sato, I., Urai, M., 2005. Detection of traces of pyroclastic flows and lahars with satellite synthetic aperture radars. Int. J. Remote Sens. 26 (9), 1927–1942.

Torres, R., Snoeij, P., Geudtner, D., Bibby, D., Davidson, M., Attema, E., Potin, P., Rommen, B., Floury, N., Brown, M., Navas, I., Deghaye, P., Duesmann, B., Rosich, B., Miranda, N., Bruno, C., L'Abbate, M., Croci, R., Pietropaolo, A., Huchler, M., Rostan, F., 2012. GMES Sentinel-1 mission. Remote Sens. Environ. 120, 9–24. https://doi.org/10.1016/j.rse.2011.05.028.

UNISDR, 2013. Global Assessment Report on Disaster Risk Reduction: From Shared Risk to Shared Value: The Business Case for Disaster Risk Reduction. UNISDR, Geneva, Switzerland.

Valerio, E., De Luca, C., Lanari, R., Manzo, M., Battaglia, M., 2022. The August 2019 Piton de la Fournaise (La Réunion Island) eruption: analysis of the multi-source deformation pattern detected through Sentinel-1 DInSAR measurements. Remote Sens. 2022 (14), 1762. https://doi.org/10.3390/rs14071762.

Veci, L., Lu, J., Prats-Iraola, P., Scheiber, R., Collard, F., Fomferra, N., Engdahl, M., 2014. The Sentinel-1 toolbox. In: Proceedings of the IEEE International Geoscience and Remote Sensing Symposium (IGARSS), Quebec City, QC, Canada, 13–18 July 2014, pp. 1–3.

Wadge, G., Scheuchl, B., Stevens, N., 2002. Spaceborne radar measurements of the eruption of Soufrière Hills volcano, Montserrat. Geol. Soc. Lond. Mem. 21 (1), 583–594.

Wadge, G., Cole, P., Stinton, A., Komorowski, J.C., Stewart, R., Toombs, A.C., Legendre, Y., 2011. Rapid topographic change measured by high-resolution satellite radar at Soufriere Hills volcano, Montserrat, 2008-2010. J. Volcanol. Geotherm. Res. 199 (1–2), 142–152. https://doi.org/10.1016/j.jvolgeores.2010.10.011.

Wadge, G., Saunders, S., Itikarai, I., 2012. Pulsatory andesite lava flow at Bagana Volcano: Geochemistry, Geophysics. Geosystems 13 (11).

Wakeford, Z.E., Chmielewska, M., Hole, M.J., Howell, J.A., Jerram, D.A., 2019. Combining thermal imaging with photogrammetry of an active volcano using UAV: an example from Stromboli, Italy. Photogramm. Rec. 34, 445–466. https://doi.org/10.1111/phor.12301.

Walter, T.R., Subandriyo, J., Kirbani, S., Bathke, H., Suryanto, W., Aisyah, N., Dahm, T., 2015. Volcano-tectonic control of Merapi's lava dome splitting: the November 2013 fracture observed from high resolution TerraSAR-X data. Tectonophysics 639, 23–33.

Walter, T.R., Harnett, C.E., Varley, N., Bracamontes, D.V., Salzer, J., Zorn, E.U., Bretón, M., Arámbula, R., Thomas, M.E., 2019. Imaging the 2013 explosive crater excavation and new dome formation at Volcán de Colima with TerraSAR-X, time-lapse cameras and modelling. J. Volcanol. Geotherm. Res. 369, 224–237.

Wang, T., Poland, M.P., Lu, Z., 2015. Dome growth at Mount Cleveland, Aleutian Arc, quantified by time series TerraSAR-X imagery. Geophys. Res. Lett. 42 (24), 10,614–610,621.

Weissel, J., Czuchlewski, K., Kim, Y., 2004. Synthetic aperture radar (SAR)-based mapping of volcanic flows: Manam Island, Papua New Guinea. Nat. Hazards Earth Syst. Sci. 4 (2), 339–346.

Werninghaus, R., Buckreuss, S., 2009. The TerraSAR-X mission and system design. IEEE Trans. Geosci. Remote Sens. 39, 873–884.

Wittmann, W., Sigmundsson, F., Dumont, S., Lavallée, Y., 2017. Post-emplacement cooling and contraction of lava flows: InSAR observations and a thermal model for lava fields at Hekla volcano, Iceland. J. Geophys. Res. Solid Earth 122 (2), 946–965.

Xu, W., Jónsson, S., 2014. The 2007–8 volcanic eruption on Jebel at Tair island (Red Sea) observed by satellite radar and optical images. Bull. Volcanol. 76 (2), 1–14.

Xu, W., Xie, L., Aoki, Y., Rivalta, E., Jónsson, S., 2020. Volcano-wide deformation after the 2017 Erta Ale dike intrusion, Ethiopia, observed with radar interferometry. J. Geophys. Res. Solid Earth 125, e2020JB019562. https://doi.org/10.1029/2020JB019562.

Zebker, H.A., Rosen, P., Hensley, S., Mouginis-Mark, P.J., 1996. Analysis of active lava flows on Kilauea volcano, Hawaii, using SIR-C radar correlation measurements. Geology 24 (6), 495–498.